BRNO UNIVERSITY OF TECHNOLOGY

VYSOKÉ UČENÍ TECHNICKÉ V BRNĚ

FACULTY OF ELECTRICAL ENGINEERING AND COMMUNICATION

FAKULTA ELEKTROTECHNIKY
A KOMUNIKAČNÍCH TECHNOLOGIÍ

DEPARTMENT OF THEORETICAL AND EXPERIMENTAL ELECTRICAL ENGINEERING

ÚSTAV TEORETICKÉ A EXPERIMENTÁLNÍ ELEKTROTECHNIKY

OPTIMIZING IMAGE RECONSTRUCTION IN ELECTRICAL IMPEDANCE TOMOGRAPHY

OPTIMALIZACE REKONSTRUKCE OBRAZU V ELEKTRICKÉ IMPEDANČNÍ TOMOGRAFII

DOCTORAL THESIS SUMMARY

TEZE DIZERTAČNÍ PRÁCE

AUTHOR   Ing. Jan Dušek

AUTOR PRÁCE

SUPERVISOR   doc. Ing. Jan Mikulka, Ph.D.

ŠKOLITEL

BRNO 2021

ABSTRACT

The thesis discusses the optimization of algorithms that reconstruct images of specific conductivity from data acquired via electrical impedance tomography. In this context, the author provides a brief mathematical description of the forward and inverse tasks, characterizes relevant data acquisition procedures, and outlines available numerical tools. Procedurally, the initial working stages involved analyzing the methods for optimizing those parameters of the model that influence the reconstruction accuracy; demonstrating approaches to the parallel processing of the algorithms; and proposing a survey of available instruments to acquire the data. The obtained knowledge then yielded a process for optimizing the parameters of the mathematical model, thus allowing the model to be designed precisely, based on the measured data; such a precondition eventually reduced the uncertainty in reconstructing the specific conductivity. When forming the numerical model, the author investigated the possibilities and overall impact of combining the open and closed domains with various regularization methods and mesh element scales, considering both the character of the reconstruction error and the computational intensity. A complementary task lay in parallelizing the reconstruction subalgorithms by using a graphics card. The results of the thesis are directly reflected in a reduced reconstruction uncertainty and accelerated computation via parallelized algorithms. The actual research benefited from an in-house designed automated tomography unit.

KEYWORDS

Electrical impedance tomography, optimization of domain parameters, electrode placement, current patterns, conductivity, data acquisition unit

ABSTRAKT

Tato disertační práce pojednává o optimalizaci algoritmů pro rekonstrukci obrazu měrné vodivosti z měřených dat pořízených elektrickou impedanční tomografií. Danou problematiku zde vymezuje stručný matematický popis dopředné a inverzní úlohy, metodika měření a pořizování dat a přehled dostupných numerických nástrojů. Uvedenou charakteristiku rozšiřuje rozbor optimalizací parametrů modelu ovlivňujících přesnost rekonstrukce, způsoby paralelního zpracování algoritmů a souhrn dostupných zařízení pro měření dat. Na základě získaných poznatků byla navržena optimalizace parametrů matematického modelu, která umožňuje jeho velmi přesný návrh dle měřených dat. V této souvislosti dochází ke snížení nejistoty rekonstrukce konduktivity. Pro zefektivnění procesu získávání dat bylo navrženo zařízení k automatizaci tomografie s důrazem na snížení nejistoty měření. V oblasti tvorby numerického modelu byly dále zkoumány možnosti užití otevřených a uzavřených domén pro různé metody regularizace a hrubost sítě, a to s ohledem na velikost chyby rekonstruované konduktivity a výpočetní náročnost. Součástí práce je také paralelizace subalgoritmů rekonstrukce s využitím grafické karty. Předložené výsledky mají přímý vliv na snížení nejistoty rekonstrukce a urychlení výpočtů paralelizací algoritmů, přičemž výzkum byl podpořen vlastním návrhem jednotky pro automatizaci tomografie.

KLÍČOVÁ SLOVA

Elektrická impedanční tomografie, optimalizace parametrů domény, rozmístění elektrod, proudové vzory, konduktivita, měřicí jednotka

Contents

Introduction

This doctoral thesis discusses current challenges in electrical impedance tomography (EIT), a relatively new non-destructive and non-invasive diagnostic method that, thanks to its properties and capabilities, is advantageously applied in various fields of technology. An acceptable cost and practical design of the equipment then make EIT an inexpensive and effective data acquisition technique.

In functional terms, the method applies an AC current to an electrode system. The electrodes are usually placed equidistantly on the border of the examined object (domain), except in geophysical measurement. The voltage is commonly measured on the non-current carrying electrodes, and the relevant values correspond to the magnitude of the flowing current and the conductivity or impedivity distribution inside the domain. Based on the obtained results, the inverse task is processed and the inverse image calculated. The spatial resolution of the reconstructed image is improvable by increasing the number of electrodes.

The outlined properties enable EIT to be employed in a variety of technical fields and activities, such as biomedicine [1], material engineering [2], monitoring of chemical processes [3], and geophysical mapping [4].

One of the topical problems in EIT rests in optimizing algorithms with respect to image reconstruction; functionally, the optimization can be carried out through novel numerical methods (e.g., the non-iterative D-Bar method with scattering transformation), precise FEM modeling (domain deformation, electrode placement, contact impedance), suppressing undesired changes in the tomographic domain (e.g., during breathing), and eliminating the measurement uncertainties (such as the stability of the current sources, and phase shift sensing). The thesis focuses on the precise FEM-based modeling, for which an optimization process using EIDORS library was designed. The numerical solution is correlated with the laboratory experiments, where the optimization functionality is verified.

The thesis contains relevant experiments and results executed or otherwise acquired within cooperation between the Faculty of Electrical Engineering and Communication and the Faculty of Civil Engineering, Brno University of Technology. Additionally, the experimental part of the work presents the deterministic methods practised during the author's internship at Netrix (Net-Art) Reseach and Development center, Lublin, Poland.

1 Electrical impedance tomography

Electrical impedance tomography (EIT) is a diagnostic method to estimate the conductivity distribution in examined objects. To illustrate the concept of the technique in general terms, we can imagine a domain having a pre-defined shape, electrodes on the boundary, and material properties. The principle lies in feeding a pair of electrodes with an AC current and sensing the voltage on the non-current-carrying electrodes. Relevant data then enable us to perform the image reconstruction. The EIT-based procedure comprises two main processes: the forward and the inverse tasks [5, 6].

The forward task calculates the voltage on the electrodes with respect to the given conductivity. In practice, this task is unambiguous and could be replaced with experimental laboratory measurement. By contrast, the inverse task is a non-linear, ill-posed problem which estimates conductivity distribution inside a domain. More specifically, the small changes occuring at the beginning of the process produce significant errors in the conductivity distribution [7, 8].

1.1 Mathematical formulation

The mathematical formulation of EIT was derived from Ampere's law and Faraday's law of induction in the differential form. The product of the derivation leads to the Laplace equation, which describes the behavior of an electric potential inside the domain, reading

$$-\nabla(\sigma\nabla\varphi) = \quad 0, \tag{1.1}$$

where σ is a conductivity, and φ denotes a potential.

The solution of the equation is supposed to be in accordance with the Dirichlet and Neumann conditions on the domain's boundary [9, 10].

1.2 Forward task

The forward task computes the voltage on the electrodes according to the examined conductivity. The task is best described by means of a complete electrode model (CEM). The numerical solution exploits discretization, and the partial differential equations (PDEs) are aproximated via the finite element method (FEM) to yield the following equation:

$$\varphi(x) = \sum_{e}\sum_{n}\varphi_{e,n}(x)W_{e,n}(x,y), \tag{1.2}$$

where $\varphi(x)$ is the electric potential, $\varphi_{e,n}(x)$ denotes the potential in the nodes of the mesh, and $W_{e,n}(x,y)$ represents a basis function to facilitate the approximation [5, 9, 11].

1.3 Inverse problem

The inverse problem is defined as an ill-posed (and thus difficult to solve) mathematical task. The principle of the problem rests in computing an objective function. The function of the least squares method (LSM) is mathematically defined as

$$\mathbf{\Psi}(\sigma) = \min \frac{1}{2} \sum \|\mathbf{U}_{\mathrm{M}} - \mathbf{U}_{\mathrm{FEM}}(\sigma)\|^2, \tag{1.3}$$

where $\mathbf{\Psi}(\sigma)$ is an objective function related to the specific conductivity, $\mathbf{U}_{\mathrm{M}}$ represents the vector of the voltages measured on the boundary, and $\mathbf{U}_{\mathrm{FEM}}(\sigma)$ denotes the vector of the voltage values computed via the forward task [6, 8].

Applying the bare LSM to the inverse problem is insufficient, especially due to the actual ill-conditioning. To increase the stability and convergence of the reconstruction, a mathematical supplement, namely, regularization, is required. In the role of examples, we list here the most common approaches to regularize the problem: Tikhonov regularization, the total variation method, NOSER[1], and the Laplace filter. All of these items are contained in the numerical tool EIDORS[2] [12], and some will be briefly discussed below. As regards the first option, i.e., Tikhonov regularization, the focus is on expanding the objective function to give

$$\mathbf{\Psi}(\sigma) = \min \frac{1}{2} \sum \|\mathbf{U}_{\mathrm{M}} - \mathbf{U}_{\mathrm{FEM}}(\sigma)\|^2 + \alpha \|\mathbf{R}\sigma\|^2, \tag{1.4}$$

where α is the regularization parameter, and $\mathbf{R}$ denotes the regularization matrix [6]. The stability and sensitivity of the Tikhonov technique depend on the regularization parameter α and also on the initial conductivity value [7, 13].

Another of the techniques, NOSER, relies on calculating only one step of the image reconstruction, utilizing Newton's method. This procedure is often employed in difference imaging, exploiting the linearized model

$$\mathbf{U} \approx \mathbf{U}(\sigma_{\mathrm{ref}}) + \mathbf{J}(\sigma - \sigma_{\mathrm{ref}}) + e, \tag{1.5}$$

where $\mathbf{U}(\sigma_{\mathrm{ref}})$ denotes the matrix of the voltage values obtained through the forward solution; $\mathbf{J}$ indicates the Jacobian, i.e., the sensitivity matrix of the forward task, and this in turn is evaluated at the conductivity σ_{ref}; and e stands for a randomly generated value expressing the noise [13, 14].

By contrast to the deterministic approaches (regularizations), there are also stochastic techniques utilizing neural networks or genetic algorithms. An artificial neural network (ANN) is based on exciting neurons and combining basic fuctions, e.g., addition, multiplication, and Boolean logic operations, to solve complex problems. An ANN has a simple algorithmic structure but requires a long procedure of prior learning. The process of machine learning rests in evaluating the outputs in relation to the neuron weight changes located at individual layers, until the required accuracy is achieved [15, 16, 17].

---

[1]Newton's One Step Error Reconstructor

[2]Electrical Impedance tomography and Diffuse Optical tomography Reconstruction Software

An alternative to ANNs is embodied in genetic algorithms (GAs), which evolve a population via initialization, selection, crossover, and mutation. The structure is sequential and is launched until the convergence criterion has been met [18, 19]. In EIT, various GAs are available, including modified variants and adaptive differential algorithms with a circular topology [20, 21, 22].

1.4   Inverse crime

The inverse task comprises ill-posed features that limit the algorithm's capability of delivering accurate reconstruction. From the perspective of EIT, we introduce here some *inverse crimes*, these being illegal ways to simplify and reduce the ill-posedness [23, 24]. Such steps are characterized as follows:

- using one and the same forward model in both simulating the data and executing the reconstruction;
- not adding simulated noise to the synthetic data;
- showcasing the reconstruction of a few special cases that produced reliable results and claiming these to represent the general performance;
- tuning the reconstruction parameters manually, using prior knowledge of the correct answer, and not presenting any blind trials, where the parameters cannot be "tweaked" (e.g., teaching a neural network by utilizing solely a training set).

1.5   Measurement strategies: current patterns

The data acquisiton mode depends on the system of electrodes and the feeding method. This subchapter presents the most common drivings for an open or a closed domain.

A closed domain is a system with electrodes equidistantly distributed on the domain perimeter. A very traditional example of such a setup is the adjacent stimulation pattern (ASP), whose principle rests in injecting immediately neighboring electrodes while leaving the others to carry out the voltage sensing. Another current driving option is the opposite stimulation pattern (OSP). Procedurally, the technique installs the feeding electrodes on the opposite side, with the other electrodes left to perform the voltage sensing. By way of an alternative, we can use Skip-X patterns, where a selected number of electrodes X is skipped between the current-carrying electrodes. To complement the discussed single-source methods, experts in the field have designed multi-source driving, namely, the trigonometric stimulation pattern, which relies on multiple independent sources capable of creating a homogeneous current density inside the domain [6, 9, 25].

The open domain setup can be demonstrated on geophysical mapping, where the electrodes are pinned to the ground equidistantly in a line or a matrix, usually on one side of the domain. A simple option is Wenner driving, exploiting dipole-dipole feeding and sensing. An alternative approach lies in the Schlumberger method. If the equidistant

and symmetrical configuration is employed, the Schlumberger concept passes into the Wenner scheme. Other current patterns are discussed in references [9, 26].

1.6 Complete electrode model parameters

The number of parameters accurately estimable is small, mainly due to the ill-posedness of the inverse problem. The individual parameters can be optimized through an *a priori* operation, using a forward solver and clearly defined physical and numerical domains. The parameters that affect the inverse imaging include boundary deformation, electrode misplacement, imprecise electrode surface, and contact impedance. The domain parameters related to the stimulation patterns are summarized in the table below [27].

Tab. 1.1: Comparing the stimulation patterns in terms of the individual parameters and current injection requirements [28].

Parameter	Adjacent	Opposite	Trigonometric
Sensitivity at the domain boundary	✓	✗	✓
Sensitivity in the middle of the domain	✗	✓	✓
Required VCCS output voltage	Low	Higher	Higher
Sensitivity to electrode position	High	High	Mid
Impact of contact impedance	Negligible	Negligible	High
Sensitivity to domain shape	High	High	Mid
Sensitivity to electrode surface	Low	Low	High
Electrode noise interference	High	High	Low
Uniform current density	✗	✗	✓
Signal to noise ratio	Low	Low	High
Multiple current sources	✗	✗	✓

1.7 Approaches to solving the domain parameters

In the real-world environment, most of the individual parameters are unknown; some, however, can be directly measured or computed before or during the reconstruction. The concepts currently available for evaluating the domain parameters are outlined below.

The compensation of skin contact impedance was studied in article [29] via a novel construction of the electrodes. The researchers fabricated compound electrodes, in which the feeding and the sensing components operated separately within one compact unit. The effect of unknown contact impedance was further investigated in sources [30, 31]. The proposed procedure was compared with a measurement. The results showed that the distributions of the conductivity and contact impedance are inseparable and cannot be estimated without a measurement using a uniform conductive medium. A method for compensating variable electrode contact was introduced in [32]. The researchers

developed a hybrid reconstruction algorithm, utilizing the CEM. The procedure indicates - and significantly reduces - artifacts caused by poor contact.

Another technique to reduce the unknown domain boundaries error was characterized in [33]. The concept exploits the Bayesian approximation error approach. The results showed that the method ensures efficient compensation, and this outcome was also verified through an experimental measurement with a KIT 4. An optimization of the electrode position at different domain shapes was devised in [34]. The method allowed fine-tuning the electrodes by solving the Fréchet derivative of the CEM, and the researchers incorporated it into the output of the LSM. The proposed algorithm facilitated simultaneous reconstruction of the conductivity distribution and electrode locations. A simultaneous estimation of the conductivity and electrode contact impedances was formulated in [35]. The method exploited Toeplitz matrices to identify bad contact and was validated via a measurement on a homogeneous vessel.

Various electrode placement options were studied in [36]. The researchers proposed an optimality criterion derived from the Bayesian approach, approximating the posterior density of the conductivity by linearizing the current-to-voltage map of the CEM. A further research on imprecise electrode modeling, electrode movement artifacts, and surface movement reconstruction was detailed in source [9]. Another procedure for optimizing the electrode position was introduced in [37]; the researchers employed an ANN to resolve electrode misplacement, exploiting EIDORS. The algorithm was validated by means of noisy simulated voltage measurements.

2 Aims and objectives

The practical section of the thesis contributes to electrical impedance tomography in the following research subdomains, problems, and tasks:

- *Reducing the uncertainty of reconstructed conductivity distribution by optimizing the mathematical model*
    - Designing a precise physical model
    - Creating relevant parametric FEM models
    - Computing the domain parameters, including shape deformation, misplacement of the electrodes, and initial conductivity
    - Analyzing the sensitivity of the mathematical models with respect to the measurement-based inverse imaging
- *Accelerating the data acquisition process relating to unknown conductivities in laboratory and field conditions*
    - Improving the parameters in view of the existing solutions
    - Collecting the open data to be made accessible to the EIT community
- *Optimizing the parameters of the closed and the open domain models*
    - Exploring innapropriately constructed domain borders in the closed and open domains and examining their impact on the reconstructed conductivity distribution
    - Determining the relationship between mesh density, number of elements, and computational effort
    - Analyzing the convergence error according to the selected regularization approach
- *Decreasing the image reconstruction time via parallelizing the algorithms*
    - Parallelizing the individual image reconstruction steps

3 Experiments

This chapter discusses the contribution and outcomes of the thesis. The first subsection presents an optimization procedure to precisely evaluate the individual domain parameters by using EIDORS. This procedure originates from a laboratory measurement on a tomograph, and its purpose was to demonstrate the impact of the individual parameters. The subsequent subsection, 3.2, describes the designing and properties of a device to facilitate effective data acquisition; this device includes, among other components, a low impedance multiplexer and a data acquisition unit. Part 3.3 outlines the impact of an extended domain (an improved parametric model), evaluates the convergence over the mesh element scale, and classifies the normalized error convergence of the selected regularization methods. The last portion of chapter 3 then characterizes the parallelization of the algorithm, delivering also a comparison of the CPU and GPU processes.

3.1 Optimizing the domain parameters

This chapter outlines a novel approach to optimizing the domain parameters; in this context, we characterize the relevant numerical modeling and simulation, together with the laboratory measurement and applied instrumentation.

Optimizing the geometry of the model, regularity, and electrode placement fundamentally affects the image reconstruction [40]. The actual solution then lies in specifying and determining the parameters that are critical in terms of the accurate results, image artefact reduction, and computational effort. All of the items can be optimized during the inverse task, albeit at the expense of a higher computational intensity; for this reason, we decided to define in advance as many parameters as possible, via pre-calculation before launching the inverse solver [41].

In view of the purpose, the Nelder-Mead algorithm was employed as the procedure to adjust an imprecise domain setup by means of homogeneous sensing. The designed approach allowed us to verify the physical and numerical FEM models, delivering a match between the resulting vectors of the simulated and the measured voltages. The heuristically based method facilitated solving nonlinear optimization problems where the derivative of the function is unknown. In such cases, the algorithm computes the relationship between the measured voltages and the properties of the domain. The method was implemented by using EIDORS library and the relevant Matlab optimization toolbox. The procedure had been designed to improve the reconstruction accuracy and to reduce the artefacts in inverse images [41].

To facilitate the optimization, we defined the minimization function of the Nelder-Mead algorithm, yielding

$$f(p) = \frac{1}{2}\|\mathbf{U}_\mathrm{M} - \mathbf{U}_\mathrm{FEM}(p)\|^2, \tag{3.1}$$

where $f(p)$ is the minimization term of the least squares method, $\mathbf{U}_\mathrm{M}$ represents the vector of the voltage measured on the physical model of the laboratory tomograph, and $\mathbf{U}_\mathrm{FEM}(p)$ stands for the voltage on the electrodes computed via the forward task. The relevant domain is parametrized by p [41].

The implementation of the procedure is visualized in Fig. 3.1.
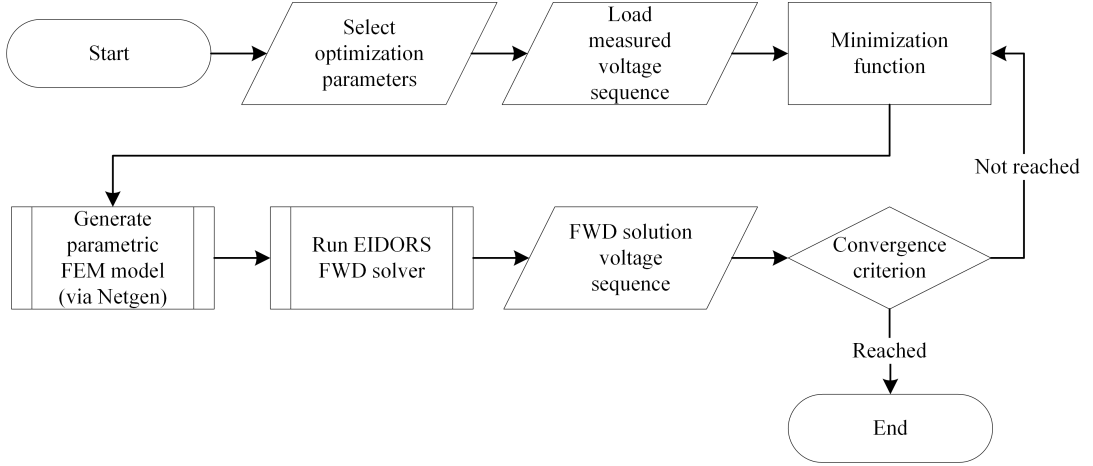
Fig. 3.1: The flowchart of the optimization procedure based on the measured dataset and selected parameters [41].

As indicated therein, the input comprises one or more selected parameters, including:

- parametric deformation of the domain boundary;
- evaluation of the initial conductivity;
- electrode location on the border of the domain.

In addition to the input parameter/s, the optimization requires the vector of measured voltages, which depends on the given current pattern; in this particular experiment, the sequence is measured on the non-excited electrodes. Exploiting the preset parameters and the voltage vector, the process initiates Netgen to generate the parametric FEM model. This model is computed via the forward task by utilizing EIDORS library [12]. The end solution then yields the voltage vector of the simulated numerical model, and the vector is evaluated by means of the optimization. If the sum of the squares reaches the convergence criterion, the optimization stops, and the return value of the function indicates the nearest possible value of the parameter preset by the user within the selected tolerance; otherwise, a new FEM model is generated and calculated [41].

Where the procedure handles multiple unknown parameters p simultaneously, the computational time becomes longer, and the algorithm may not find a correct solution.

To validate the functionality of the optimization, we employed a laboratory model with an inserted homogeneous medium; this step allowed us to verify the results physically. In addition to estimating the listed optimization parameters, the procedure has a potential to approximate the contact impedance by evaluating the sensing on the current-carrying electrodes. The actual impact of the parameters is demonstrated on inverse images that include inhomogeneities [41].

In the experiment, we used a laboratory tomograph and a corresponding numerical model (Fig. 3.2). The height and diameter of the tomograph equaled 35.5 and 19 cm, respectively. The physical model also contained electrodes equidistantly distributed along its perimeter. The individual levels were located at 13.6, 21.6, and 29.6 cm above the bottom plane of the vessel; each stage involved 16 electrodes (stainless steel bolts) with the diameter of 9 mm and height of 6 mm [41].
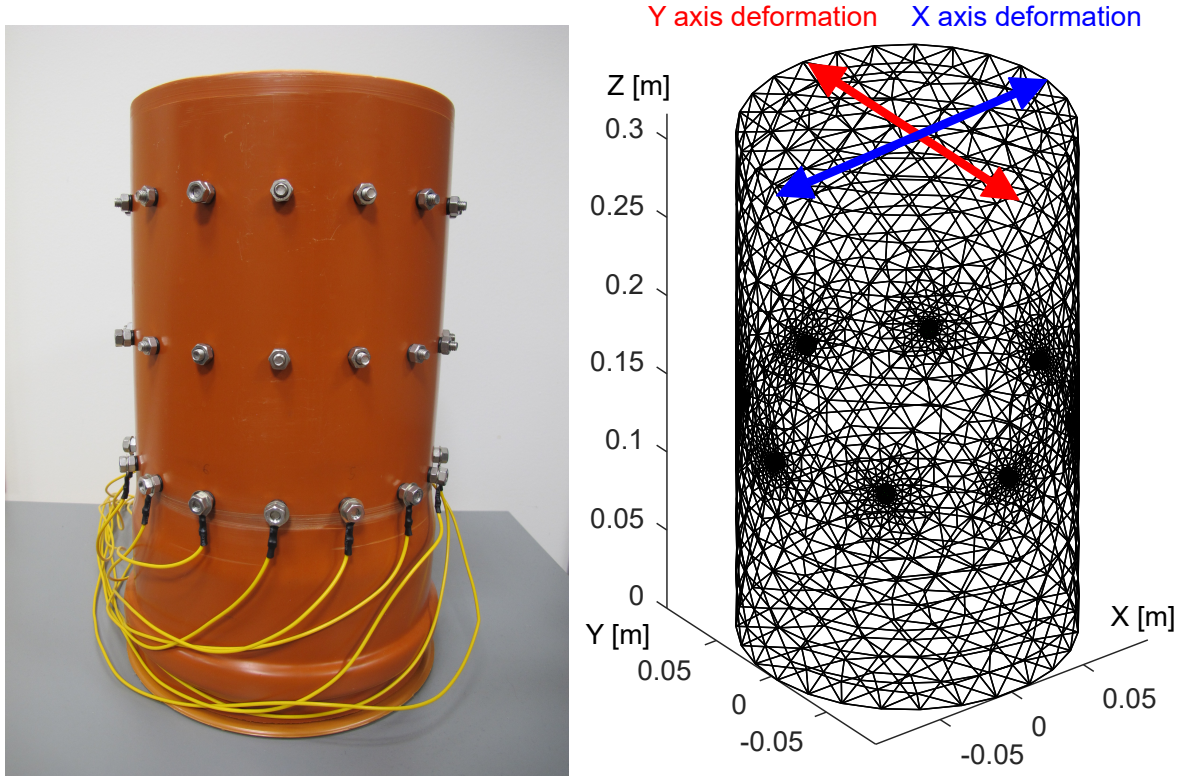

Fig. 3.2: The tomograph and the related Netgen-based numerical model [41].

To demonstrate the impact of the individual parameters on the inverse imaging, we set up an 8-electrode configuration. For the purposes of the optimization, we then prepared a corresponding, FEM-based model containing approximately 15,000 elements. The unused electrodes allowed us to form an irregular placement pattern on the domain boundary [41].

Initial conductivity

An optimal initial conductivity value constitutes a factor that simplifies the convergency of the inverse solution. We employed potable water as the medium to optimize the initial conductivity. The input data were embodied in a vector of voltages measured via the ASP and the OSP and at two tomograph shapes. The initial model was designed with respect to the real dimensions, namely, the height and the regular diameter of 0.316 m (water level) and 0.19 m, respectively; the axis diameters of X = 0.186 m and Y = 0.194 m, capturing the elliptic deformation; the electrode placement level of 0.296 m above the bottom; and the contact impedance of 10 mΩ[1], equaling the EIDORS default value. The injected current was 2.002 mA at the frequency of 1,007 Hz. To start the optimization, we employed a total dissolved solids conductometer, obtaining the conductivity value of 47.2 mS/m. The outcomes of the conductivity optimization are presented in Tab. 3.1. The setup to acquire the data is shown in the figure below [41].

Tab. 3.1: Comparing the current patterns in terms of the actual parameters [41].

Current pattern	Domain shape	Conductivity [mS/m]
Adjacent	Circular	54.4
Adjacent	Elliptic	53.7
Opposite	Circular	54.9
Opposite	Elliptic	54.2

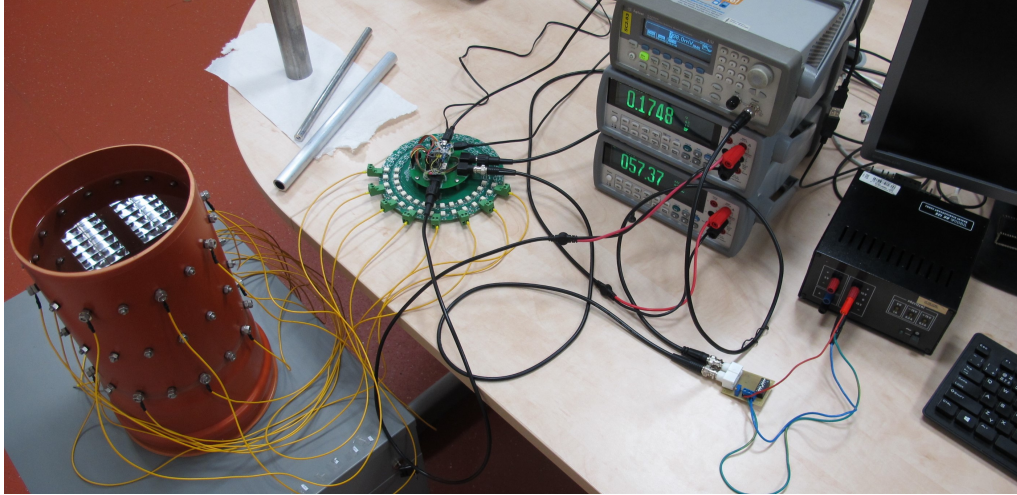$I = 2.002\,\mathrm{mA}$; $f = 1{,}007\,\mathrm{Hz}$.

Fig. 3.3: The data acquisition setup [41].

The optimization delivers the initial conductivity values (Tab. 3.1) associated with the current patterns and domain shapes. The computational intensity of the optimization reached 7 s at the maximum, while the generation of the FEM model took 3.5 s [41].

---

[1]The sensing on the non-excited electrodes was accompanied by a small current and thus a low voltage drop, leading to the conclusion that the impact of the contact impedance is almost negligible.

Shape deformation

The shape deformation influences the quality of the inverse imaging. To resolve this problem, we extended the applied procedure; in addition, we prepared the same setup as that employed in optimizing the conductivity. The procedure enabled us to evaluate the shape deformation in diameters X, Y. Within the initial step, we assigned the value of 19 cm (in each axis), thus starting with a circular shape. The variation of the diameters during the process and the inhomogeneous setup are displayed in Fig. 3.4.
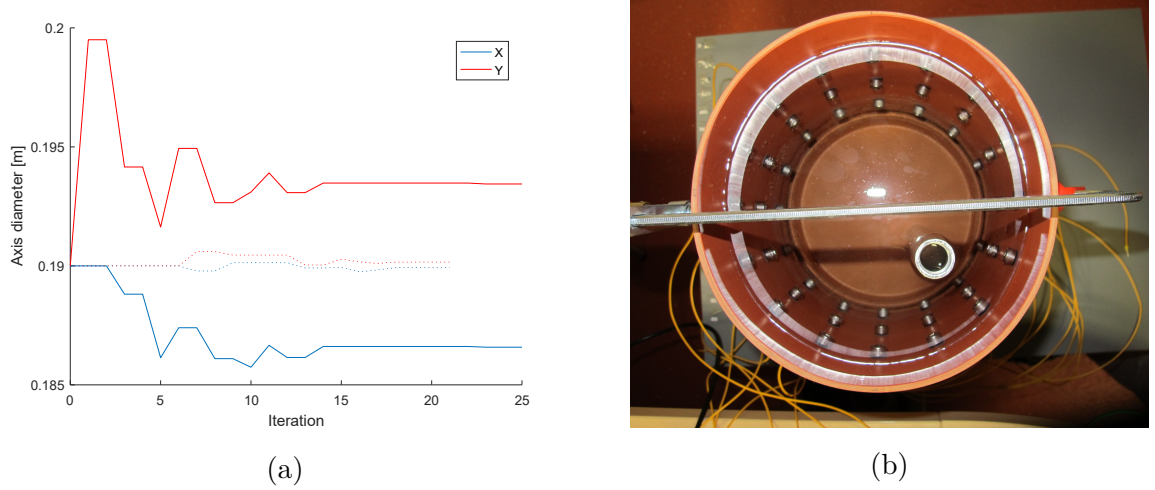

(a)   (b)

Fig. 3.4: (a) The variation of the diameters on axes X and Y, relating to the opposite pattern in the non-optimized (solid lines) and optimized (dotted lines) scenarios, and (b) the tomograph containing water and an inserted aluminum pipe [41].

In Fig. 3.4a, we characterize two different optimization scenarios: A non-optimized model where the algorithm has found the diameters of the elliptic deformation (solid lines) of the circle, and an optimization of the original, or true, scenario (dotted lines) to demonstrate the convergence ability and to specify the error of the algorithm. Based on the outputs of the homogeneous measurement, which were compared with the resulting vector of simulated voltages produced by the forward task, we calculated the shape deformation. The estimates of the optimized axis diameter equaled X = 18.62 cm and Y = 19.35 cm in the ASP and X = 18.66 cm and Y = 19.35 cm in the OSP. The values are very close to the real dimensions [18.6; 19.4]. The outcomes delivered by the OSP show that the algorithm exhibits very good robustness. The error of the diameter values was 0.1 %, corresponding to 0.2 mm on the absolute scale. The inaccuracy of the results may have arisen from insufficient precision in measuring the diameter or the voltage uncertainty. The deformation took between 205 and 250 s to optimize. The resulting diameters were employed as the inputs to perform the reconstruction (Fig. 3.4b) [41].

To demonstrate the impact of an imprecise domain shape, we reconstructed the invalid and true models, applying the ASP and OSP (Fig. 3.5). The initial conductivity had been selected from within Tab. 3.1, with the regularization parameter set to 0.001 [41].
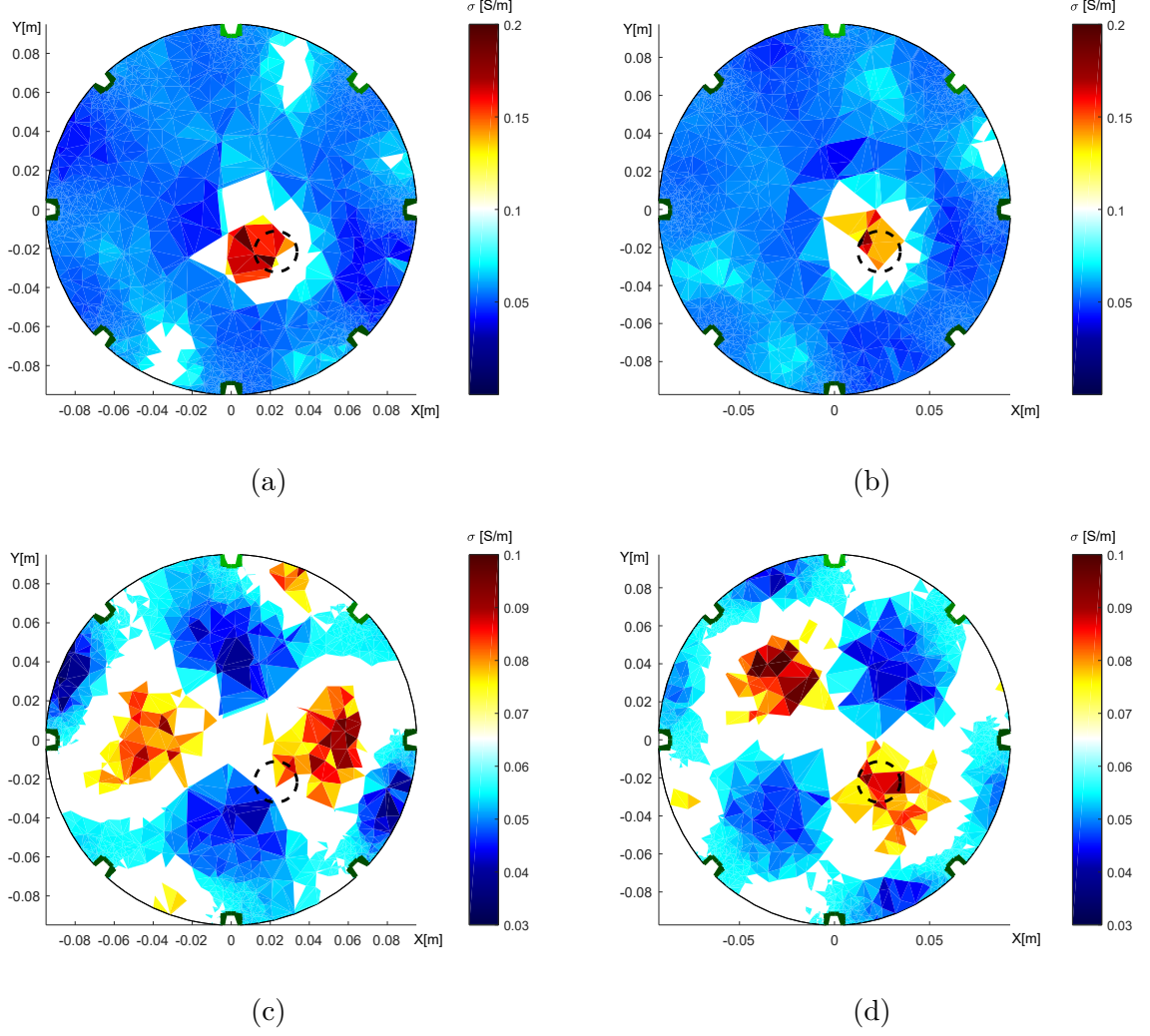
Fig. 3.5: The reconstructed conductivity distributions, obtained with ASP (top) and OSP (bottom). The tomograph's axial dimensions equal X = 18.6 cm and Y = 19.4 cm; (a,c) wrongly selected circular shapes, and (b,d) the true model of the elliptic domain [41].

The reconstructed images show the effect of the original domain model, where the imprecise domain boundary led to incorrect localization of the inhomogeneity (Fig. 3.5a). By comparison, the optimized model (Fig. 3.5b) localized the aluminium object better but still did not deliver a flawless result. This problem could be eliminated by a more parametrizable model deformable in multiple dimensions and shapes [41].

The conductivity images obtained via the OSP provided a higher sensitivity to the shape deformation. The imprecise boundary diameters (Fig. 3.5c) caused the inhomogeneous areas to rotate, unlike the conditions in the optimized model (Fig. 3.5d). Further, the inverse image exposed two higher conductivity regions, and these corresponded to the original object and artefact. The same effect was described in references [42, 43]. The object mirroring is preventable via a different sensing configuration [41].

Misplaced electrodes

Misplaced electrodes embody a major source of artefacts and inverse imaging errors within our experiments. To analyze the problem, we set the tomograph in such a manner that the 6th electrode was shifted one step nearer the 7th one (Fig. 3.6a). Before running the optimization, we decided to utilize both homogeneous water to find the position of the electrode and a heterogeneous medium to demonstrate the impact on the inverse image (Fig. 3.6b). The changing position of the electrode, related to the function count, and a top view on the optimized domain mesh in the elliptic shape are shown in Fig. 3.7 [41].
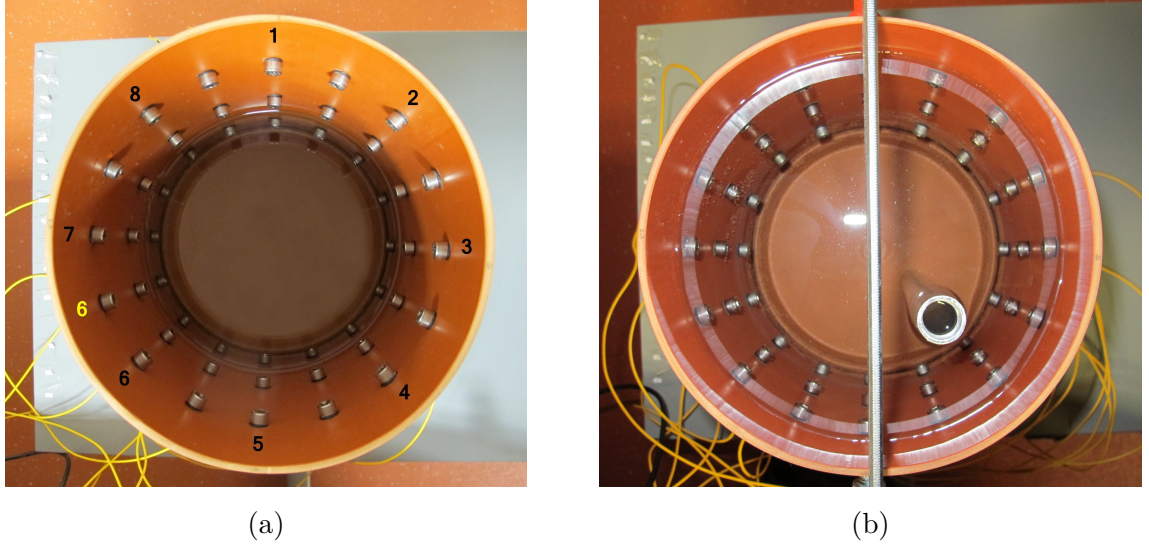

(a) (b)

Fig. 3.6: (a) The experimental setup including the shifted 6th electrode (highlighted in yellow); (b) the tomograph filled with water, comprising an aluminum object [41].
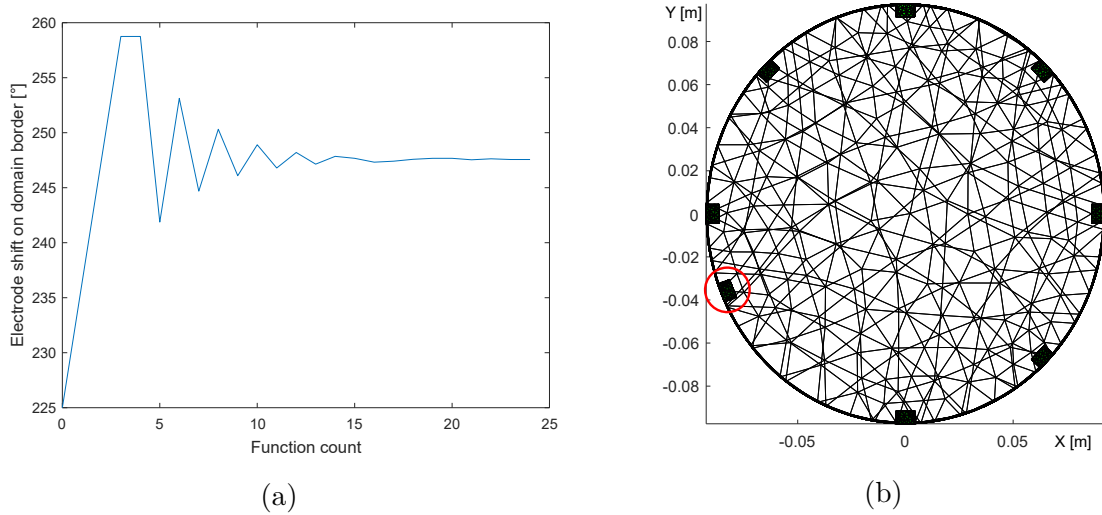

(a) (b)

Fig. 3.7: Optimizing the electrode misplacement: (a) electrode position related to the function count; (b) optimized electrode placement in the domain mesh [41].

As regards the graphical representation above, Fig. 3.7a visualizes the electrode shift, correspondingly to the changing value of the angle on the domain perimeter during the count of the optimization operations. The electrode moves along the domain boundary within the range of 225° - 260° and converges to 247.6°. The discussed procedure took between 90 and 110 s. The result of optimizing the electrode positions via ASP is presented in Fig. 3.7b. The model was solved sucessfully, with the 6th electrode shifted in the same manner as in the original model (Fig. 3.6). In addition, we performed the experiment also by means of opposite sensing (Fig. 3.8) [41].
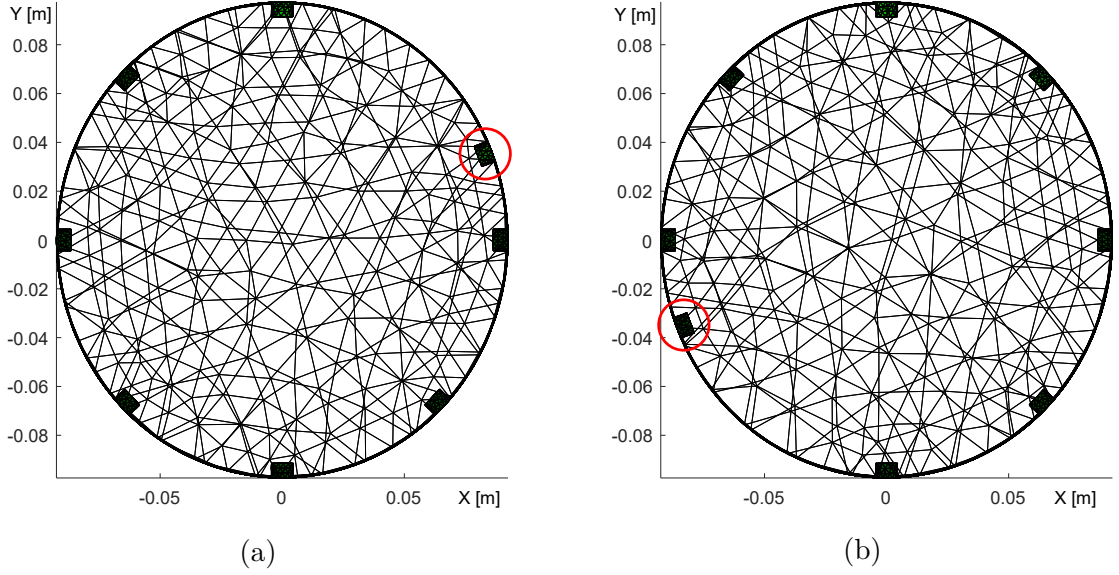

Fig. 3.8: A top view of the optimized models obtained via opposite sensing. The images display a duality of the solution ((a) the 2nd or (b) the 6th electrode shifted) [41].

The mesh on the left-hand side (Fig. 3.8a) contains the 2nd electrode evaluated at the angle of 68° with respect to the 1st electrode. The other mesh (Fig. 3.8b), by comparison, shifts the 6th electrode to 248°, the initial value being 225°. Both of the models are verified via the forward task, and the simulated voltages exhibit almost identical values. The detected duality means that the procedure had not yielded an acceptable result. Eventually, we found opposite sensing inconvenient for evaluating the electrode misplacement; the impact of the electrode positioning had been reconstructed only with the ASP (Fig. 3.9) [41].

An incorrect placement of the electrode is presented in Fig. 3.9a, together with the resulting inverse image. The reconstructed inhomogeneity was recognized wrongly, near the boundary between the 6th and the 7th electrodes. Compared to the imprecise model, the correct domain (Fig. 3.9b) includes the conductivity at the presumed position, localizing it satisfactorily. The randomly distorted conductivity areas in the reconstructed images could arise from an insufficient image resolution, limited by the number of active electrodes [41].
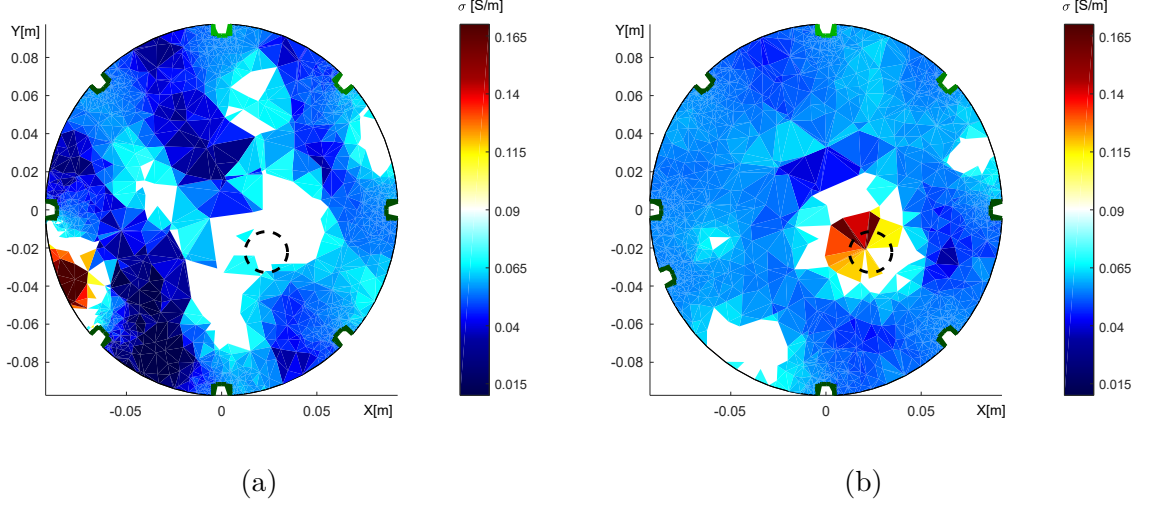
Fig. 3.9: The reconstructed conductivity distributions in the (a) inaccurate regular electrode setup and (b) correct placement of the 6th electrode [41].

Error evaluation

To evaluate the reconstructed conductivities with respect to the original setup, we sampled the images at the resolution of 256×256 pixels. The accuracy was calculated via the relative root mean square error, by using the following equation [44]:

$$RRMSE(\sigma) = \sqrt{\frac{\sum_{i=1}^{px}(\sigma(i) - \sigma_{\mathrm{orig}}(i))^2}{\sum_{i=1}^{px}(\sigma_{\mathrm{orig}}(i))^2}} \cdot 100, \qquad (3.2)$$

where $RRMSE(\sigma)$ denotes the total error in the sampled inverse image; px characterizes the number of pixels; $\sigma(i)$ stands for the reconstructed conductivity in a pixel; and $\sigma_{\mathrm{orig}}(i)$ is the original conductivity corresponding to the real measurement setup [41].

The area of the inhomogeneous object was evaluated through comparing the FEM model that represented the setup of the experiment with the one expressing the reconstructed conductivity distribution. To estimate the space of the object, we preset the experimentally established threshold to 66 % of the maximum conductivity, thus obtaining the mask to effectively separate the background from the inhomogeneity. This allowed us to compare the individual inhomogeneity areas, calculated via the equation

$$IAR_{0.66} = \frac{\sum_{i=1}^{px}(\sigma_{\mathrm{Inv}}(i))}{\sum_{i=1}^{px}(\sigma_{\mathrm{Fwd}}(i))}, \qquad (3.3)$$

where $IAR_{0.66}$ is the area ratio between the original and the reconstructed conductivity regions of the inhomogeneity in the cross-sectional image, $\sigma_{\mathrm{Inv}}(i)$ denotes the conductivity in the reconstructed image, and $\sigma_{\mathrm{Fwd}}(i)$ represents the conductivity distribution in the FEM model that corresponds to the real laboratory setup [41].

The above equations enabled us to classify the actual impacts on the domain shape (Tab. 3.2) and the electrode placement (Tab. 3.3) optimization process as regards the computed conductivity distribution [41].

16

Tab. 3.2: The image errors in the boundary deformations [41].

Current pattern	Domain shape	$RRMSE(\sigma)$ [%]	$IAR_{0.66}$ [-]
Adjacent	Circular	34.59	0.658/2.542
Adjacent	Elliptic	28.43	0.768/1.905
Opposite	Circular	51.99	0.274/5.947
Opposite	Elliptic	40.41	0.763/3.504

The measurement was performed on the elliptically deformed domain.

Tab. 3.3: The image errors in view of the electrode positioning [41].

Electrode position	$RRMSE(\sigma)$ [%]	$IAR_{0.66}$ [-]
Equidistant	52.73	0.000/1.483
6th shifted	40.04	0.667/3.124

The measurement was performed by applying adjacent driving in the elliptically deformed domain, utilizing the non-equidistant electrode setup (shifted 6th electrode).

Summary

The initial conductivity was optimized with potable water, yielding between 53.7 and 54.9 mS/m in dependence on the actual combination of the current pattern and domain deformation (Tab. 3.1). The evaluation of the procedure took 7 s at the maximum [41].

In addition, the optimizing process evaluated the boundary deformation of the circular domain. To verify the designed procedure with real data, we employed a clamp in the laboratory model to obtain a deformation of 2 %. The estimated modified diameters of the domain shapes equaled X = 18.62 cm and Y = 19.35 cm in the ASP option and X = 18.66 cm and Y = 19.35 cm in the OSP one. Considering the real axial dimensions {18.6; 19.4} of the tomograph, the optimization delivered acceptable results. Evaluating the boundary deformation took 205 to 250 s, with a significant portion of the computational effort allocated to the generation of the meshes. The impact of the imprecise boundary modeling was demonstrated via reconstructing the image from the data measured on the elliptical domain. We performed the experiment on the accurate and the incorrect circular models (Fig. 3.5). The results show an imperfect localization of the inhomogeneity compared to its original position. In both of the driving techniques, the optimized model reduced the overall conductivity distribution errors by 6.16 % and 11.58 %. In the expected region of the object, the inhomogeneity area ratio defined through equation 3.3 increased from 0.658 to 0.768 (11.0 %) in the adjacent driving option and rose from 0.274 to 0.763 (48.9 %) in the opposite pattern, the latter change being especially remarkable. The area of the object in the space of the tomograph was also evaluated by applying the inhomogeneity area ratio, with the inhomogeneity volume in the inverse image diminishing from 2.542 to 1.905 in the ASP and falling from 5.947 to 3.504 in the OSP. The outcome of the optimization then lay in that the opposite option was considerably more sensitive to the shape deformations (Tab. 3.2). We also demon-

strated the mirroring effect of opposite sensing to propose a solution which requires either complementing the measurement or selecting another sensing strategy [41].

The optimization procedure also facilitated evaluating the electrode misplacement. For this reason, we prepared the model containing the shifted 6th electrode. Observing the design of the experiment, we measured on an accurate (shifted) and an incorrect (regular, or equidistant) electrode setup of the model, via both the ASP and the OSP. The optimization had to be supported by the dataset of the homogeneous conductivity measurement. The ASP proved convenient because, unlike opposite sensing, it does not deliver an unacceptable duality. In this context, the duality means that the two different optimization products (the shifted 2nd and 6th electrodes) provide identical voltage values, which are interchangeable in the forward task (Fig. 3.8). Based on such an outcome, we decided to exclude the OSP from the optimization of the electrode misplacement. We demonstrated the impact of an inaccurate electrode location via reconstructing the conductivity with the ASP. The relationship between the recognition of the object and changes in the position of the electrode is exposed in the inverse images above. The relative root mean square error dropped by 12.69 %, and the inhomogeneity localization improved significantly, from a zero match to the similarity of 0.667 (in Tab. 3.3). The time required to compute the electrode misplacement ranged between 90 and 110 s [41].

The entire procedure was implemented by using the Matlab optimization toolbox, EIDORS tool, and Netgen mesh generator; the last of these softwares allowed us to generate the three-dimensional models. The designed scheme is suitable for adjusting the unknown parameters of the real laboratory model to create a corresponding numerical model for a precise image reconstruction. At present, the optimization solves only one parameter per run, this being one of the deficiencies; the other limitation consists in that the computational intensity grows with an increasing number of the degrees of freedom, which are computed simultaneously. The optimization concept is universal, bringing a potential to include another parameter, such as contact impedance; this capability is important in analyzing the current-carrying electrodes and multisource strategies. The procedure is independent of the applied mesh generator and can utilize multiparameter models compatible with the EIDORS tool [41].

Hardware and software

The experiment exploited the following devices and software [41]:
- CPU: Intel Core i3-6098P (3.6 GHz); 16 GB RAM;
  operating system: Windows 10 (x64);
- Matlab R2016b (x64); EIDORS version 3.9;
- Keysight 34450A multimeter; Agilent DSO-X 3014A oscilloscope;
- PLI EIT system version 0.1.

3.2 Hardware for the tomographic measurement

To perform an appropriate tomographic measurement, we assembled and set up convenient instruments. Based on the information outlined in actual thesis, a prototype Precise Low-Impedance (PLI) system [41, 45] was designed, with a structure as follows:
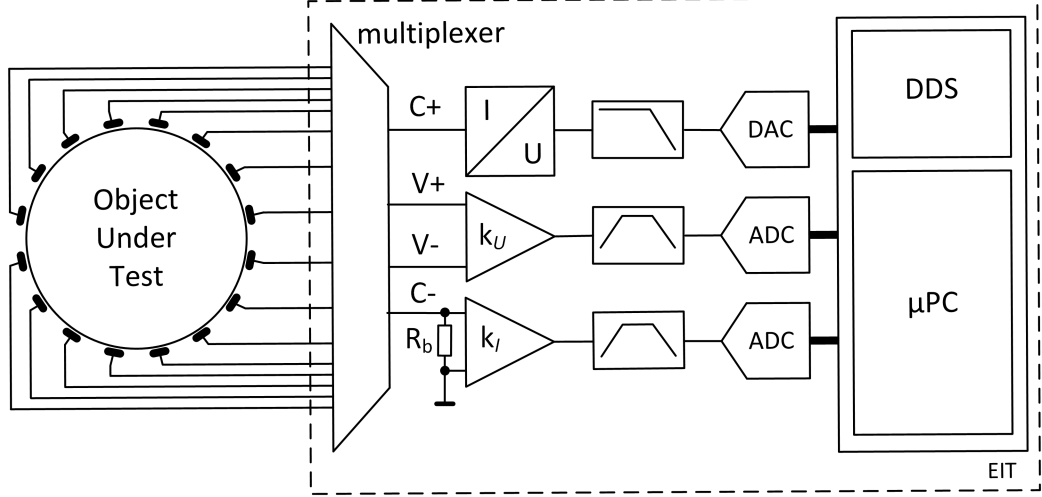

Fig. 3.10: The PLI EIT system [45].

As indicated in Fig. 3.10, the electrodes are connected to a multiplexer, which also wires them to the current source and the differential amplifiers. In our case, the source was voltage-controlled and completed with a grounded shunt to measure the voltage gap by using another amplifier. The other amplifier monitored the voltage on the electrodes of the tomograph. Additionally, bandpass filters are installed behind the amplifiers to prevent voltage drifts and instability. The filtered signal passes to an ADC. The feeding part comprises a low-pass filter and a DAC. The circuit is controlled by a microprocessor including a digital generator (DDS) to produce a harmonic signal for feeding [45].

As regards the parameters of the components (a current source, a multiplexer, and a measuring unit), the most important specifications are summarized in the table below.

Tab. 3.4: The ideal parameters of the equipment.

Parameter	Range
Frequency	10 Hz - 400 kHz
Phase shift resolution	1°
Measured voltage range	1 mV - 10 V*
Switching voltage	$\pm$ 30 V
Multiplexer on-state resistance	< 10 Ω
Switching points per plane	16*
Injection current	0 - 3 mA$_{pp}$

The symbol * indicates parameters in which further expansion is desirable.

To design a current source for the PLI EIT system, we utilized a Howland current pump including two operational amplifiers. This circuit ensured a higher output impedance and a wider frequency range compared to the basic and improved variants. In our case, the Howland pump functioned as a voltage to current converter.

Another part of the design lies in the structure of the multiplexer. To materialize the above- mentioned parameters of the device, we eventually abandoned integrated circuits due to their low operating ranges and opted for an in-house built discrete multiplexer. This component was assembled with galvanically separated switches (TLP3545A) delivering a low on-state resistance (40 mΩ) and sufficient voltage swiching (60 V) [45, 46].

To complement these system parts, we designed a unit to perform measurement and data conversion; the design of the unit is characterized in the figure below. The relevant diagram visualizes only one sensing wing because the other has the same structure.
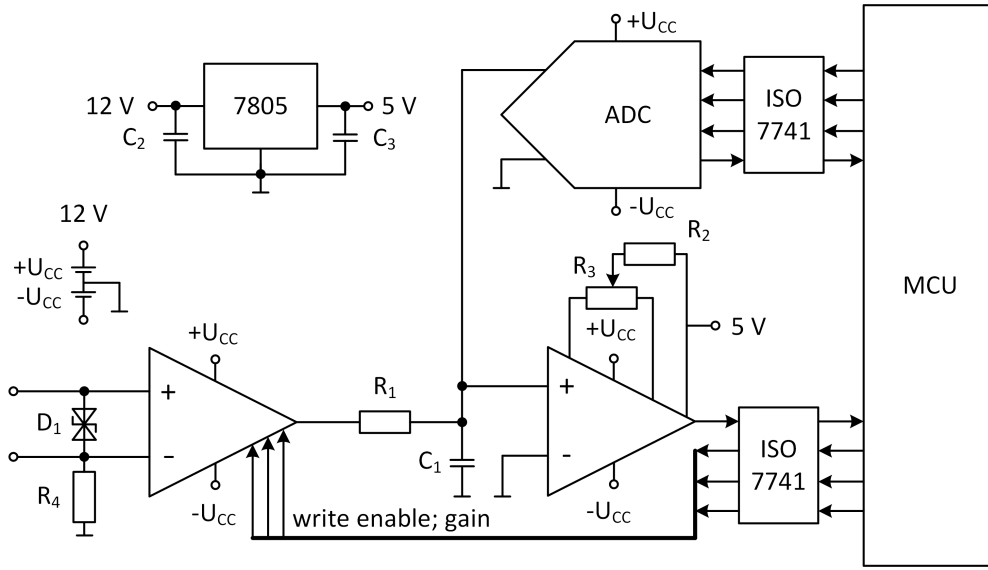

Fig. 3.11: The designed measuring branch of PLI EIT system.

The measuring unit relies on two supply values: 12 V and 5 V to feed the PGA, ADC, and hysteresis comparator. The inputs of the amplifier are directly connected to the multiplexer, a TVS diode to prevent damage to the circuit, and a resistor R_4 to create the DC feedback of the inputs with respect to the power supply. Behind the amplifier, we inserted an RC filter with a bandwidth adjusted to 440 kHz. The filter's output is connected in parallel to the ADC and the hysteresis comparator. Based on the evaluated frequency from the comparator, the MCU determines precisely the time to repeatedly measure the signal via the ADC, and the final value is specified as a mean of the individual measurements. The communication between the MCU, the PGA, the ADC, and the comparator is expected to be galvanically separated by digital isolators. The power supply is supposed to exploit isolated DC/DC converters to avoid ground loops, with an inserted LC filter on the output to suppress ripple and noise.

Results

The device is still being developed at present; thus, this section discusses only a partially assembled prototype of the PLI EIT system. The prototype contains a low impedance multiplexer; a shunt resistance; a microcontroller that manages the pairs of switching electrodes; LabView-based software; and an external VCCS. The multiplexer's impedance was verified via four-electrode measurement (Fig. 3.12).
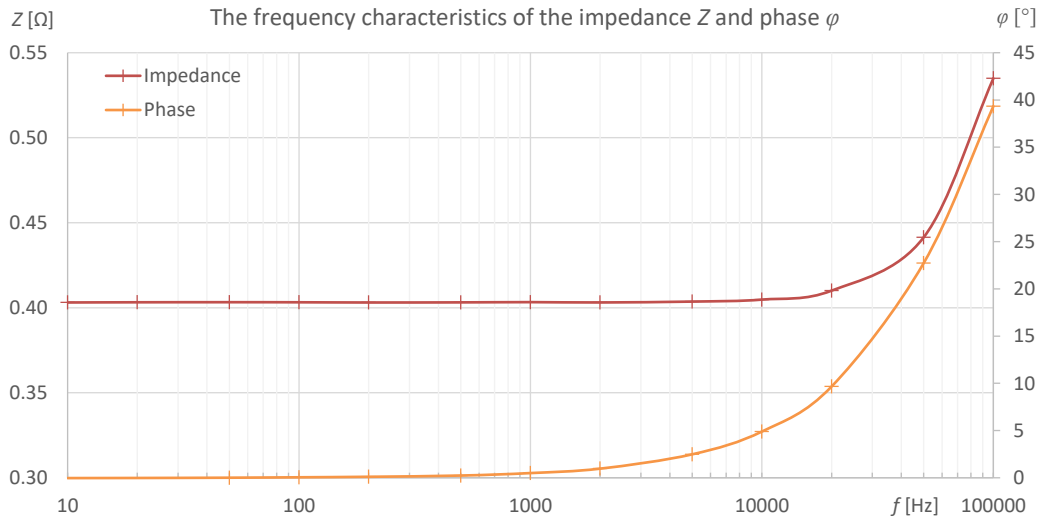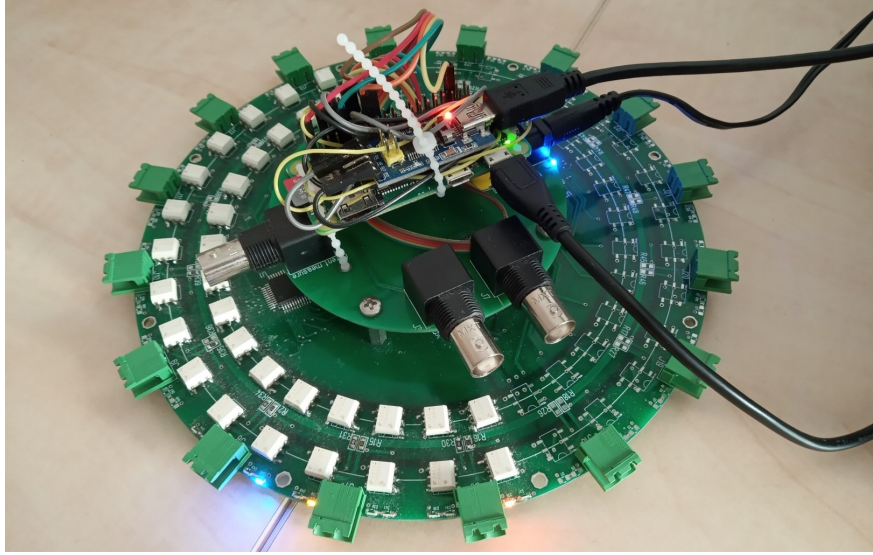

Fig. 3.12: Top: The PLI EIT prototype [45]. Bottom: The frequency characteristics of the multiplexer's impedance, and phase.

As is indicated in the figure, the impedance begins to increase at 10 kHz and rises from 0.40 Ω to 0.54 Ω at 100 kHz. The phase of the impedance then jumps from 0 to 40 degrees between 1 and 100 kHz. The impedance of the multiplexer can be considered very low (smaller than 1 Ω), and the relevant parasitic impact on the measured values is almost negligible [45, 46].

Experimental reconstruction using the PLI EIT prototype

To launch the reconstruction procedure, we employed a tomograph and the above-discussed PLI EIT prototype (the VCCS and multiplexer), which was supported by applicable laboratory devices (a function generator, digital multimeters, and an oscilloscope). The images display a diagram of the voltage and phase shift measurement circuit and visualize the setup for the inhomogeneous conductivity distribution.
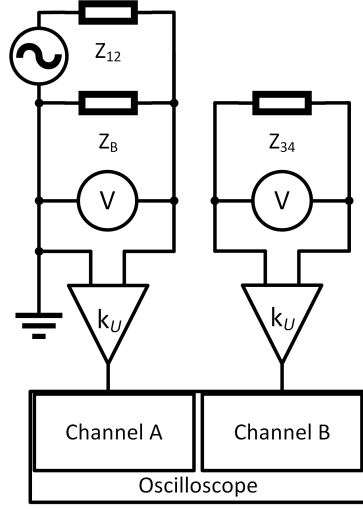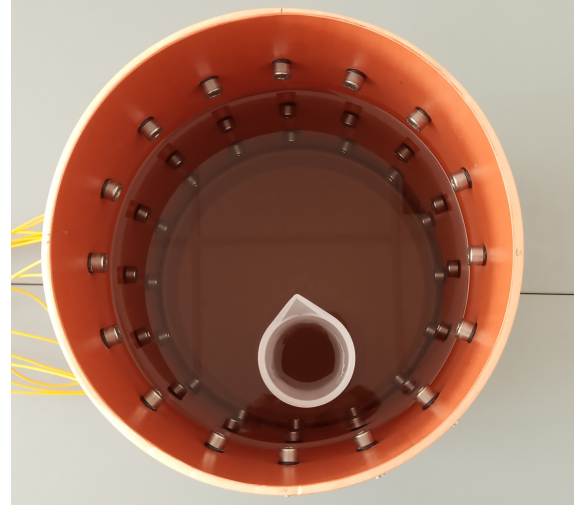
Fig. 3.13: (a) A diagram characterizing the voltage and phase shift measurement circuit; (b) the tomograph with an inserted graduated cylinder [47].

In Fig. 3.13a, we introduce the feeding and sensing wings, which are galvanically separated. The Z_{12} and Z_{34} represent the impedances between the electrodes of the tomograph. The feeding part of the circuit comprises an AC source including a function generator, and a VCCS. The AC source output was connected with the excitation electrodes through a shunt resistance ($Z_B = 10 \ \Omega$), to which we wired a voltmeter, an amplifier, and an oscilloscope. The voltmeter enabled us to control the amplitude of the injection current. Combining the amplifier and the oscilloscope then ensured the measurement of the phase shift between the feeding and the measuring branches. The measuring wing of the circuit contained the impedance Z_{34}, where the voltmeter indicated the voltage. Furthermore, the amplifier and the oscilloscope were wired in parallel to the impedance; thus, we scanned the signal to measure the phase shift for the admittivity evaluation [47].

The setup of the experiment is depicted in Fig. 3.13b, with the images showing the water-filled tomograph and the graduated cylinder inserted to generate an inhomogeneity having a pre-defined shape [47].

In the experiment, we utilized 8 electrodes arranged on a single level. The injection and sensing pattern relied on the ASP. The injected current (I_B) equaled 2.008 mA at 1,007 Hz, and the excitation current was measured on the shunt resistance (Z_B). By

extension, we measured the sequences of the voltage and the phase shift of the signals monitored under homogeneous and inhomogeneous conductivity distributions [47].

When reconstructing the image, we employed Netgen to prepare a mesh including 17,708 elements. The mesh was refined near the electrodes and boundaries, allowing us to compute the admittivity distribution more accurately. The reconstruction was performed via a difference inverse algorithm utilizing the objective function, and this algorithm involved the Gauss-Newton method complemented with a Tikhonov regularization term. The reconstructed admittivity components are visualized in Fig. 3.14 [47].

(a)   (b)
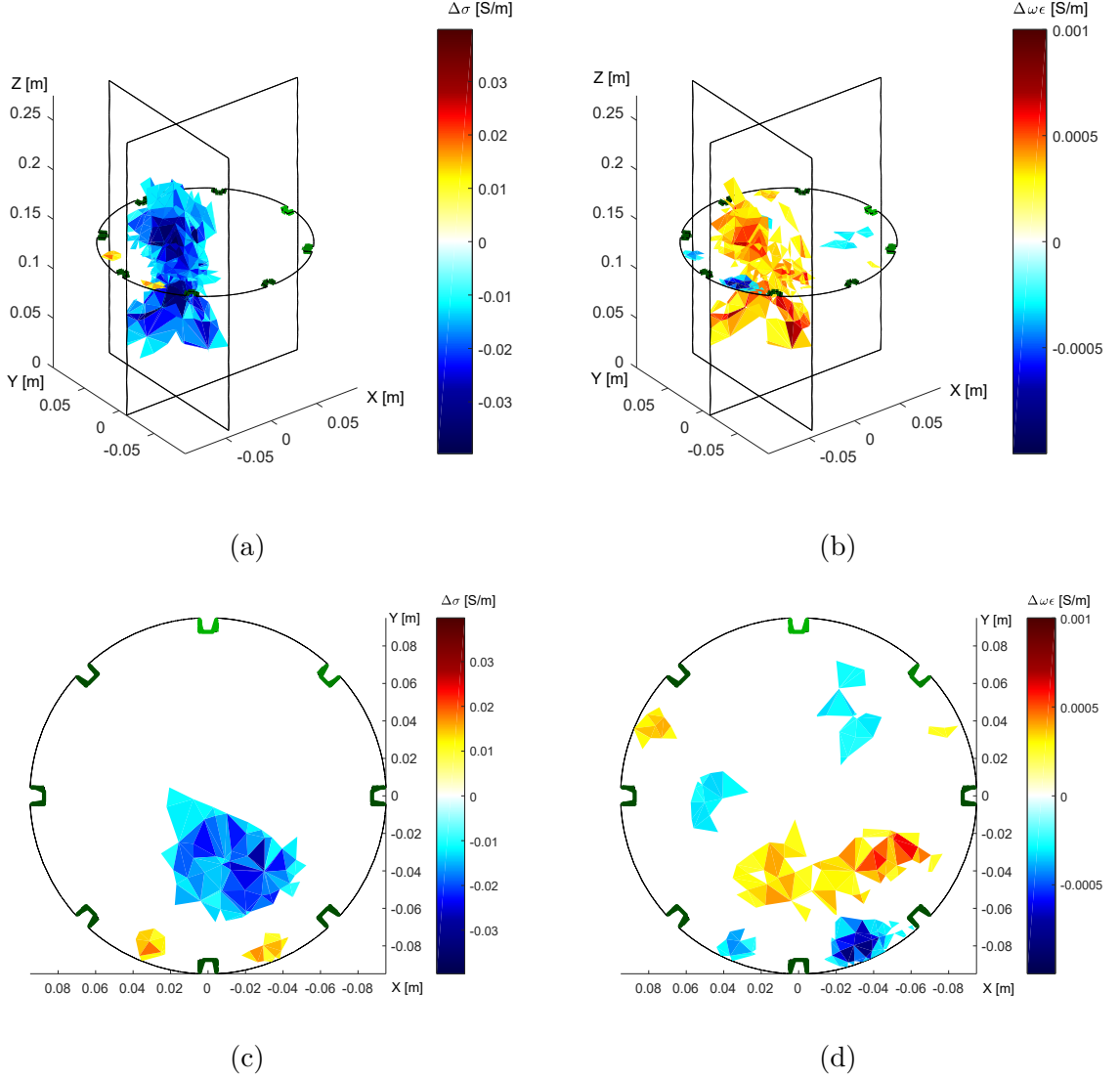
(c)   (d)

Fig. 3.14: The reconstructed difference in the admittivity distribution: 3D cross-sectional images (top), and two-dimensional cross-sections at the electrode level (bottom) [47].

The cross-sectional images (Fig. 3.14a, 3.14c) of the conductivity indicate an inhomogeneity region around the coordinates [-0.01; -0.04]. The 3D cross-section comprises a vertical expansion; this effect was expectable, as the reconstruction process utilizes only one level of electrodes, and the object then extends beyond the scanning plane [47].

23

The imaginary part of the admittivity is represented in Fig. 3.14b and 3.14d, where the three-dimensional cross-section resembles that characterizing the conductivity. Thus, the imaginary component too exhibits a major vertical expansion, mainly due to the actual concept of the experiment. In view of the reconstruction results, the object can be described as weakly capacitive (see the red band). The cross-section at the electrode level (Fig. 3.14d) contains weakly inductive areas represented by blue patterns; these elements arise from the measurement error. In addition, the resulting cross-section includes a randomly distributed capacitive area near the original position of the object; generally, this capacitive region appears to be shapeless, meaning that its form does not entirely match that of the inserted cylinder. Such an error is most probably caused by the small phase difference between the measured phase values of the homogeneous and the inhomogeneous states on the one hand and the character of the graduated cylinder, which acts as an insulator, on the other. Another factor probably rests in the non-shielded cables that connected the tomograph and multiplexer [47].

The reconstructed cross-sectional images were defined at the electrode level and then evaluated by using the Jaccard index and the mean absolute value. The Jaccard index characterized the location of the inhomogeneity. In the specific conductivity, the values of the index and the mean square error equaled 0.8498 and 1902.5, respectively, while those of the imaginary component corresponded to 0.5837; 8994.7 [47].

The experiment showed that the PLI EIT system is suitable for data acquisition in EIT. The device can still be improved in terms of, for example, the shielded cables and active electrodes. Furthermore, the overall results also revealed that the conductivity has a major impact on determining the position and approximate size of the object. By comparison, the imaginary component cannot provide enough position-related information; this deficiency stems from several factors, including but not limited to the amplitude and frequency of the excitation current and the different electrical properties of the medium and the inserted cylinder. Such factors cause the phase between the injected current and the measured voltage to be almost unmeasurable, making the reconstruction of the imaginary part very problematic [47].

The sensing sequence, involving 40 voltage values, took approximately 90 seconds. The most time-consuming activity lay in the measurement performed with the applied laboratory devices (2 seconds per value). In the 16-electrode configuration, which we had not used practically, the assumed data acquisition time reached approximately 500 - 550 s. Thus, by contrast to the manual cycle, the time to obtain the data was theoretically reduced from 3 hours to less than 10 minutes, improving the process significantly.

To enable the discussed experiment, we utilized the following hardware:

- PLI EIT version 0.1 (multiplexer, VCCS);
- Agilent 33220A function waveform generator;
- Keysight 34450A 5½digit multimeter;
- Agilent DSO-X 3014A four channel oscilloscope.

3.3 Error exploration in the open and closed domains

A correct mesh model is of fundamental importance in EIT imaging due to FEM calculations. The main challenge lies in achieving a compromise between the size of a mesh element and the computational cost. For this reason, we evaluated the *a posteriori* convergence of the imaging algorithms; the mesh element size; and the computational effort for the open and closed domains. The analysis was performed by using the EIDORS tool, which comprises the Gauss-Newton algorithm and regularizations. The error was evaluated with a minimum mean squared error, a sum squared error, and the Jaccard distance. To evaluate the convergence error, we designed the procedure in Fig. 3.15, with the domains generated by using the GMSH tool [48].
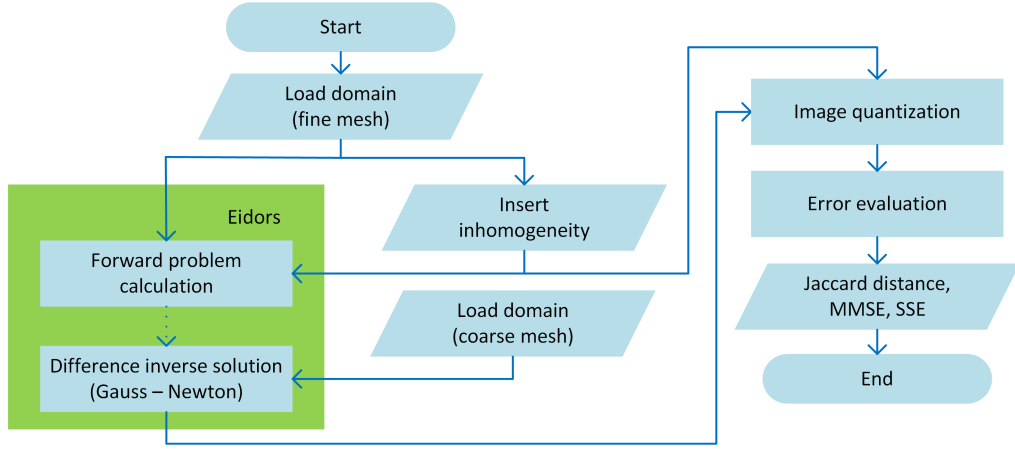

Fig. 3.15: The individual stages in evaluating the domains [48].

In the initial phase, we generated an unstructured fine mesh to constitute the original domain. This domain was processed via the forward task to obtain the data of the homogeneous medium. Subsequently, we inserted an inhomogeneity into the domain and calculated the inhomogeneous data. These operations were performed separately because we employed a difference inverse solver to carry out the reconstruction. To avoid an *inverse crime*, we prepared a coarse mesh. At the next stage, we applied the Gauss-Newton method expanded with the Laplace, NOSER, and Tikhonov regularizations, thus obtaining the results that facilitated a comparison of the algorithms. The reconstructed and the original domains were quantized and saved as an image having a regular grid. The results were then evaluated by the Jaccard distance, the sum of squared errors (SSE), and the minimum mean square error (MMSE) [48].

Before the simulation, we fixed the forward solver and random noise to ensure comparable results (the same sequence of voltage values). The closed domain mesh covered the range of 62 to 20,408 elements, and the open domain encompassed 160 to 19,958 elements. Examples of the closed and the open domain designs with inserted inhomogeneities and reconstructed conductivities are shown in Fig. 3.16 [48].
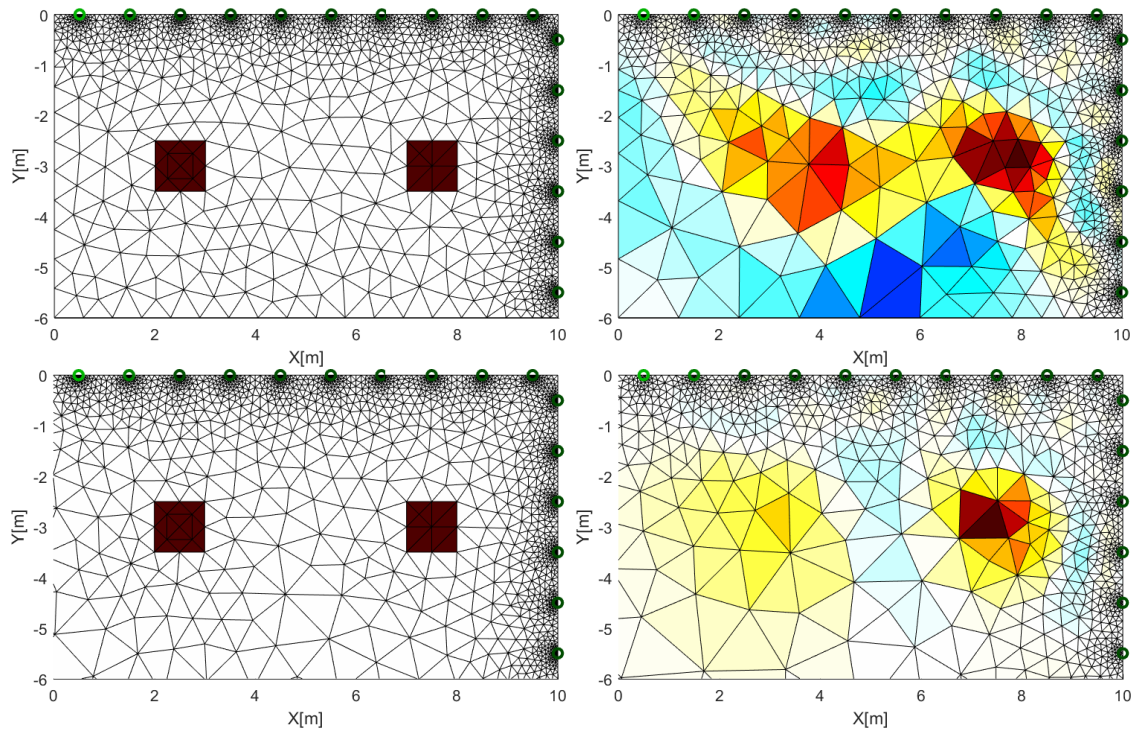
Fig. 3.16: The reconstruction in the closed (top) and the open (bottom; zoomed to detail at the regions of interest) domains, executed via the Gauss-Newton method including the Tikhonov penalty [48, 49].

The relationship between the computational time and the mesh element scale with respect to the Gauss-Newton method and the different regularizations, observed in both the open and the closed domains, is illustrated in Fig. 3.17.

Fig. 3.17: The relationship between the number of mesh elements and the computational time in the selected reconstruction methods [48].

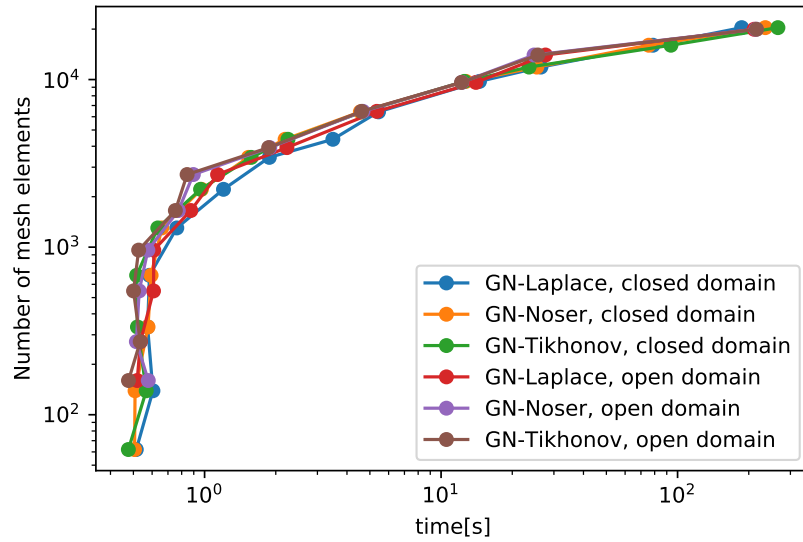As is shown in Fig. 3.17, the applied regularization technique does not have a significant impact on the computational intensity. The difference between the open and the closed domain models was almost negligible. Based on these results, the selected regularization and the mesh design appear to be stable for the purposes of the Gauss-Newton inversion. By extension, the image above also relates the convergence behavior of the inversion to the increasing number of elements and mesh complexity given by the specific hardware. The actual convergence estimation normalized into the range of 0 to 1 is displayed in Fig. 3.18 [48].

Summary

In the closed domains, the optimum range to enable the Tikhonov inversion was identified between 500 and 1,000 elements; here, the Jaccard distance, MMSE, and SSE achieved the best results in terms of the computational intensity. Generally, in the same context, NOSER proved to be more stable and suitable for a wider range of mesh element scales, albeit only at the cost of a decreased quality of the inverse image. The Laplace regularization then delivered the worst results. As regards the open domain, the most convenient method was Tikhonov, especially if employed in the area of 2,700 elements, where it ensured acceptable computational intensity. A good compromise lay with NOSER: This algorithm offered a stability markedly better than Tikhonov's and operated in a wider range of selected meshes, but the inversion accuracy did not match the results delivered by the Tikhonov in this respect. In the Laplace method, we observed a high variation of the normalized error scale, and, by extension, the highest absolute value [48].

The discussed experiment was calculated on a standard computer with an Intel Core i3-6089P 3.60 GHz processor and 4 GB RAM. The software, i.e., the EIDORS tool and GMSH mesh generator, ran on OS Win 10 x64, under Matlab R2016a [48].
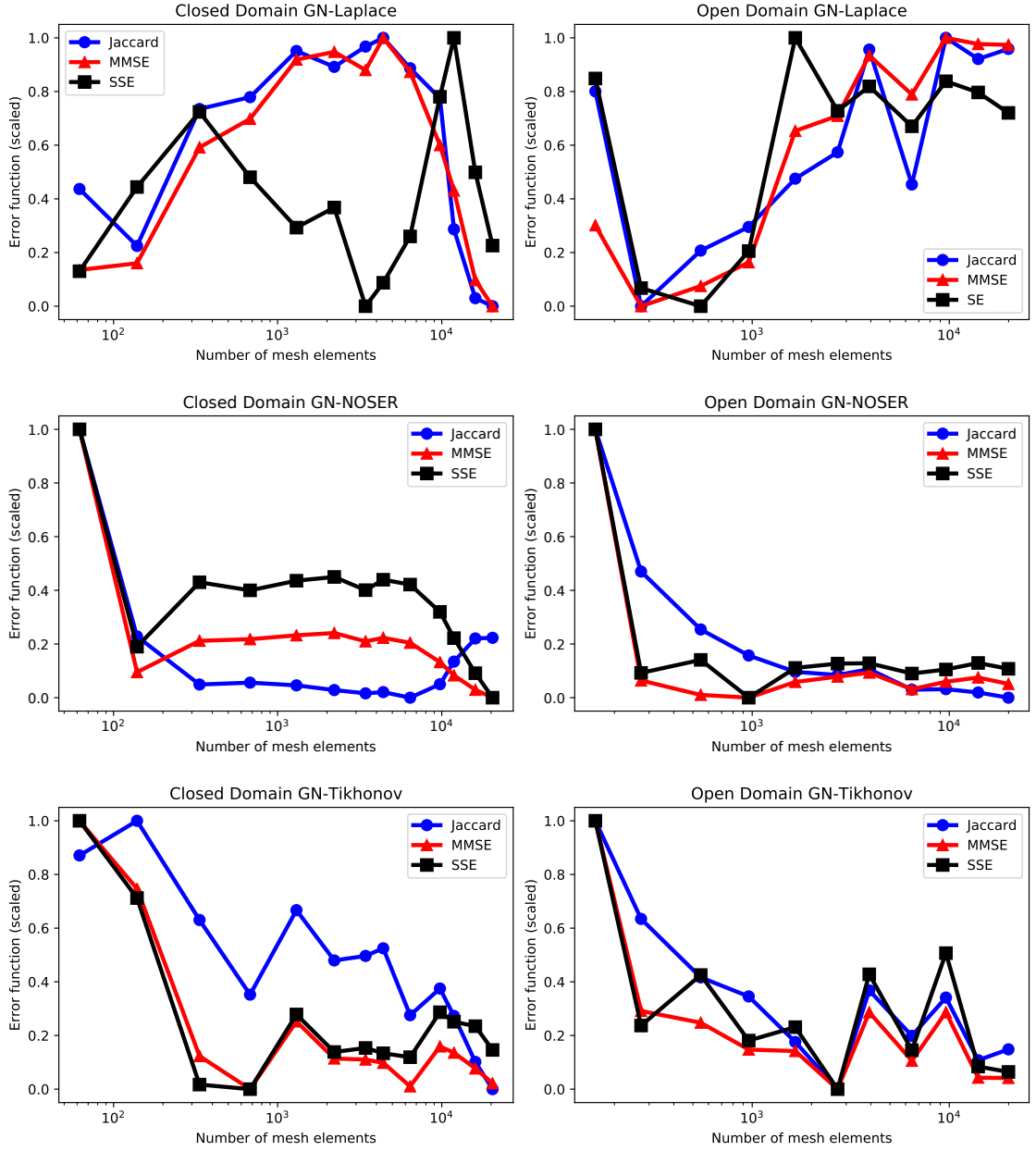
Fig. 3.18: The error convergence estimates normalized in the range of 0 to 1, characterizing the closed (left-hand column) and the open (right-hand column) domains and considering the numbers of mesh elements and regularizations [48].

3.4 Parallelization

One of the most prominent challenges in EIT imaging lies in reducing the computational intensity of the solution. For this reason, we parallelized the algorithm designed by Vauhkonen in Matlab [50]. In our case, the first procedural phase involved computing the Jacobian because this part embodies the most time-consuming part of the calculation. At the next stage, we substituted the sequential CPU code in the parallel solution via the CUDA function processed by the GPU (Fig. 3.19). The relevant computational times are compared in Tab. 3.5. The results show that the parallel processing is approximately twenty times faster than the sequential approach [51].
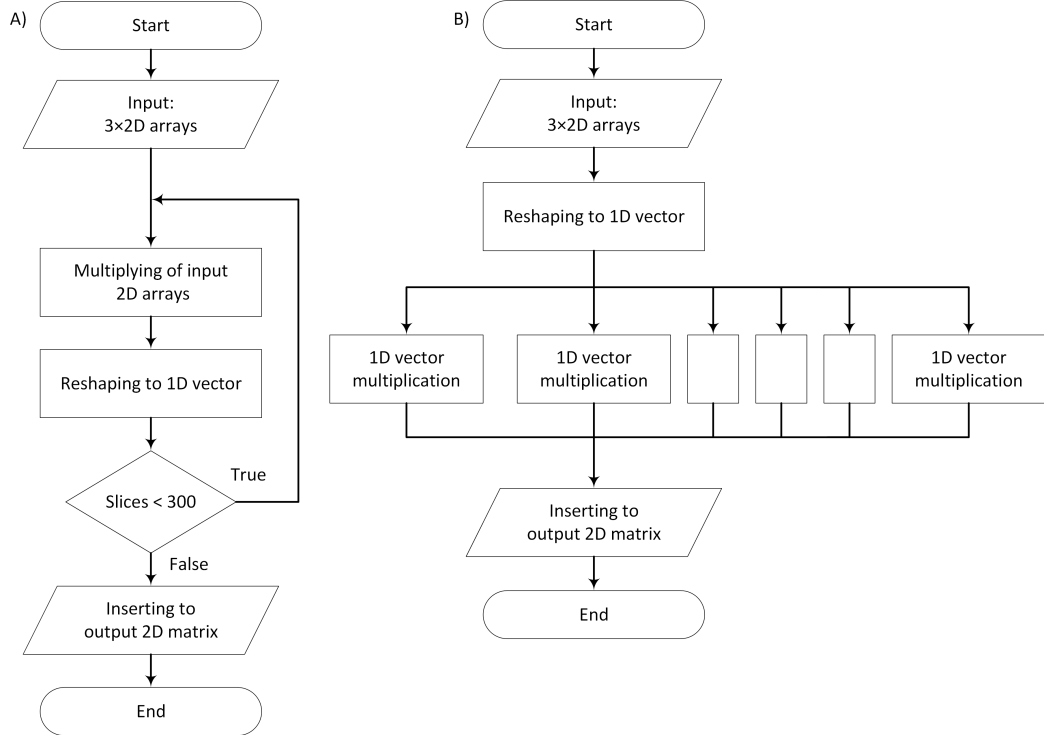
Fig. 3.19: The A) sequential and B) the parallel implementations of the Jacobian [51].

Tab. 3.5: Comparing the Jacobian computing procedures [51].

Hardware	Time [ms]
CPU: Intel Core i5-4460 (3.2 GHz; x64; 8 GB RAM)	5
GPU: NVIDIA GTX 970 (1.215 GHz; memory 4 GB)	0.25

Based on the results specified above, we decided to run the whole EIT image reconstruction process on a CUDA platform to reduce the time cost. The most time-consuming portion of the image reconstruction (the Jacobian) had been successfully implemented in the previous phase, for which we had selected the Gauss-Newton approach, including the Tikhonov penalty. The CPU and GPU-based options are visualized in Fig. 3.20 [52].

Fig. 3.20: The flowcharts of the differently processed forward and inverse tasks [52].

Tab. 3.6: The computing times in the reconstruction via CPU and GPU [52].

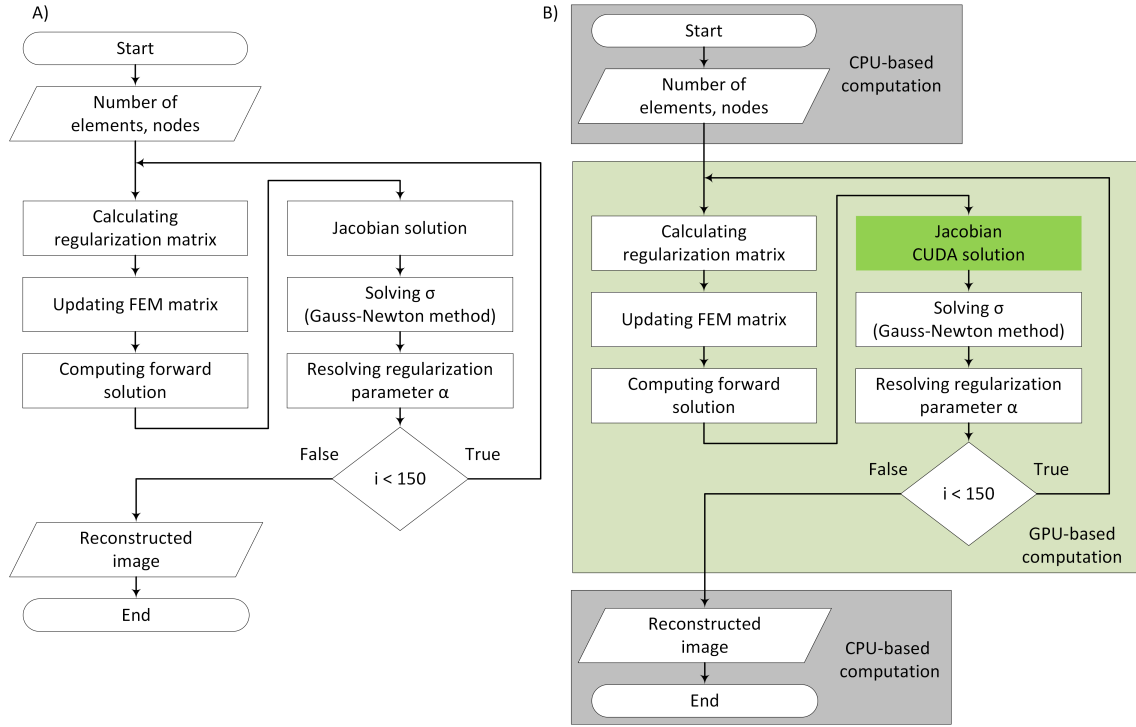| Process	CPU time [ms]	GPU time [ms]
Calculating the regularization matrix	1.6	1.3
Updating the FEM matrix	4.3	0.9
Forward solution	0.7	6.0
Computing the Jacobian	20.6	0.1
Solving σ with the Gauss-Newton method	1.6	7.5
Total time per iteration	**28.8**	**15.8**

As indicated, the GPU option is superior in terms of the total time per iteration. The *calculating the regularization matrix* item exhibited a slightly reduced overall time consumption thanks to multiplying the 1D vector and the regularization matrix; *updating the FEM matrix* proved to be faster, and greater differences are assumable at increasing numbers of elements; *forward solution* significantly slowed down in the parallel processing, due to the RAM - VRAM data transfer caused by an unsupported *symamd* function; the CUDA-based code of the *Jacobian* was computed almost two hundred times more quickly than that of the original CPU processing; and *solving σ* markedly increased the computational intensity, due to the matrix division. The sequential behavior of the process had most prominently decelerated the GPU-based implementation [52].

The experiment utilized an Intel Core i5-4460 CPU (3.2 GHz; x64; 8 GB RAM), NVIDIA GTX 970 GPU (1.215 GHz; memory 4 GB), Win 10 (x64), and Matlab R2016a.

Discussion

Optimization

The applied optimization procedure can reduce the image reconstruction uncertainty in three different ways, depending on the choice. The first step rests in evaluating the initial conductivity from the sequence of measured voltages. For this reason, we prepared a corresponding cylidrical FEM model containing approximately 15,000 elements and 8 electrodes. The initial conductivity value reached between 53.7 and 54.9 mS/m. The designed procedure converges very fast and, with the computer and experiment employed in this thesis [41], takes 7 s at the maximum.

In addition, the proposed approach also facilitates calculating the boundary deformation of the elliptical domain, considering the dimensions of the {X, Y} axes. The designed procedure was verified on real data acquired from a laboratory tomograph deformed with a clamp. By optimizing the shape deformation, we yielded the centimeter lengths of {18.62, 19.35} and {18.66, 19.35} in adjacent and opposite driving, respectively. In the real axial dimensions of X = 18.6 cm and Y = 19.4 cm, our approach delivered acceptable results (the relative axis value errors amounted to {0.31 %, -0.25 %}). The impact of an innacurately modeled shape was also demonstrated on an image reconstruction involving wrongly constructed circular and true elliptical domain shapes, where the relative root-mean-square error dropped by 6.2 % and 11.6 % in the adjacent and the opposite current patterns, respectively [41].

The optimization also allowed evaluating the electrode position on the domain boundary. For this reason, we prepared a model containing a shifted 6th electrode, which was then monitored with the adjacent and the opposite patterns. The optimization produced suitable results in the adjacent measurement and a non-acceptable duality in the opposite sensing strategy. The duality had arisen from the two possible electrode placement options (the shifted 2nd and 6th electrodes), where the forward solver provided a sequence with the same, interchangeable voltage values (Fig. 3.8). Thus, we present the impact of an electrode misplacement only on the adjacent pattern, via inverse images (Fig. 3.9) of the innacurate and the correct models. The optimization reduced the relative root-mean-square error by 12.7 %; the inhomogeneity localization was significantly improved too, from a mismatch to the Dice similarity of 0.667 [41].

The procedure was implemented by using the Matlab Optimization toolbox, the EIDORS tool, and the Netgen mesh generator. Overall, the approach is suitable for adjusting the unknown parameters of the real laboratory model to create a corresponding numerical model that will enable precise image reconstruction. The current limitations rest in that only one parameter is solvable per run and that the computational intensity markedly increases due to the rising number of degrees of freedom being computed simultaneously. The optimization design is universal and yields a potential to include another parameter, such as contact impedance [41].

Newly proposed system

Accelerating the data acquisition process in laboratory and other in- and outdoor conditions is based on identifying and exploring a device for automatized data collection. The first step to reach this goal lies in specifying the key parameters of such a device. To reduce the time to obtain the tomographic data of the laboratory model, we proposed a setup comprising a multiplexer, a voltage-controlled current source, and a microcontroller-regulated circuit to operate the feeding and the sensing branches. The multiplexer was materialized in a discrete manner, utilizing a shift register connected into a combination of photorelays with a low on-state resistance (lower than 1 Ω). The VCCS was built on a multirange Howland current pump. This design enabled us to control the injection current either through the amplitude of the input voltage or manually, by switching the resistors placed before the voltage follower. The presented multiplexer and VCCS were verified via an experimental measurement on a laboratory tomograph that allowed the actual image reconstruction. The results showed that the assembled device is suitable for obtaining EIT imaging data. The setup facilitated research into the optimization procedure and reduced the time required to obtain the tomographic data from hours to minutes. The device for effective data acquisition in EIT (a precise, low impedance EIT system) is being refined within diverse Bachelor's projects supervised by the author of this thesis [45, 46, 47].

Error exploration in the open and the closed domains

The experiment centered on designing the open and the closed domains was performed by using EIDORS library, which contained different regularizations, namely, Tikhonov, NOSER, and Laplace. To explore the errors, we generated domain meshes consisting of 62 to 20,408 elements. The computational time for the specified mesh element scale remained stable (0.4 s - 0.5 s) between 60 and 1,000 elements but then began to rise (0.5 s to 300 s), with a gradual increase in the number of elements from 1,000 to 20,000 [48].

The reconstructions for the domains were performed by utilizing the results of the *a priori* calculated forward solution and the fixed random seed facilitating the noise data generation. The Jaccard distance, minimum mean square error, and sum squared error were selected to evaluate the inverse images. The results of the designed simulation process relating to the above-mentioned regularization approaches are summarized in Tab. 3.7.

Tab. 3.7: The regularization approaches compared in terms of the Jaccard distance, MMSE, and SSE over the mesh element scale.

Regularization	Jaccard distance	MMSE	SSE	Mesh element range
Tikhonov	0.30 - 0.40	0.03 - 0.06	300 - 550	2,000 - 16,000
NOSER	0.44 - 0.48	0.06 - 0.09	400 - 600	500 - 20,000
Laplace	0.60 - 0.65	0.19 - 0.28	950 - 1,150	60 - 20,000

The table presents the Tikhonov method as the one with the smallest values of the error metrics; the stability, however, was not perfect. A good alternative to the Tikhonov option was found in NOSER, whose capabilities ensured an enhanced stability at a wider scale of mesh elements. This tool nevertheless also produced a slightly higher error than the Tikhonov procedure. Considering the selected techniques, the worst results were delivered by the Laplace term; the reason apparently lies in that the output depends on the *a priori* conductivity information, which had not been involved in the experiment. Such conditions then yielded amplified noise and decreasing solution stability in the Laplace regularization [48].

In terms of the computational effort (approximately 0.5 s), the best area for the image reconstruction involving the close domains was identified in the vicinity of 800 elements. The open domain model provided the best results in the range of 2,600 to 3,000 elements, considering the inverse image quality and time consumption (between 1 s and 2 s). The experiment was performed on a standard personal computer, described in detail at the end of section 3.3 [48].

Parallelizing the algorithms

The parallelization of the algorithm created by Vauhkonen [50] indicates that the GPU-based implementation is positively faster than the original sequential Matlab code. To compare these two options, we employed a FEM model containing 300 elements, 167 nodes, and 16 electrodes. The experiment was carried out by applying trigonometric driving and the injection current of 1 mA. The final computational time reached 28.8 s and 15.8 s in the CPU and the GPU-based variants, respectively. The most significant improvement in the inverse task processing was eventually achieved in the Jacobian, with the time intensity falling from 20.6 s to 0.1 s. The individual procedural steps had comprised functions not supported by the GPU processing, and these slowed down the computation. In the given context, the forward solution proved to be hampered by the data transfer between the RAM and the VRAM, namely, the unsupported *symamd* function, and solving the conductivity of the Gauss-Newton iteration appeared problematic due to the matrix division performed during the solution of the system of linear equations. Further exploration generated the possibility of another decrease in the computational effort; the potential to reduce this factor lies in the GPU implementation of the unsupported *symamd* function [51, 52].

Conclusion

The results outlined in the thesis, the Discussion chapter in particular, contribute significantly to EIT research worldwide, especially by

- **decreasing the uncertainty of the reconstructed conductivity distribution via optimizing the mathematical model through a set of laboratory measurements [40, 41];**
- **accelerating the data acquisition in laboratory and other in- and outdoor conditions [45, 46, 47];**
- **optimizing the parameters of the closed and the open domain models (mesh density, computational effort, and analysis of the convergence error) [48, 49];**
- **improving the time intensity of the image reconstruction via parallelizing the individual algorithm steps [49, 51, 52].**

The central target fields and activities comprise, above all, multidisciplinary provinces such as geophysical mapping and exploration, laboratory equipment design and testing, and the optimization or analysis of multiparametric models to reduce the uncertainty in reconstructed conductivities. The newly obtained concepts are applicable in automating data acquisition tasks and conducting diverse laboratory practicals at technical universities, inclusive of the specialized measurement and electromagnetic field modeling courses delivered at the Faculty of Electrical Engineering and Communication, Brno University of Technology.

The outcomes presented herein relate back to the author's internship at Netrix (NetArt) S.A. Research and Development Center, Lublin, Poland, and his participation in science seminars at University of Economics and Innovation in Lublin and at Warszaw University of Technology. By extension, the thesis contains the products of a project (junior grant FAST/FEKT-J-18-5385) executed in cooperation with the Department of Water Structures, Faculty of Civil Engineering, Brno University of Technology. The relevant research involved experimental measurement of inhomogeneities inserted in water and soil, and the findings were published in [53, 54].

The future efforts will be pursued in collaboration with the above-specified institutions, the target fields and activities being effective data sensing, exploration of the open domain models, application of neural networks to the EIT problem, and improvement of the existing optimization procedure to include the contact impedance parameter and a multiparametric model with irregular boundaries.

The results of the experiments were published in the MDPI Sensors journal (impact factor 3.275 (Q2) [41]), Elektrorevue peer-reviewed journal [54], and international and national conference proceedings (Eureka [40, 46, 53], ICUMT [45], Mechatronika [47], IIPhDW [48, 52], EEICT [49], PIERS [51]).

Bibliography

[1] BOVERMAN, G., T.-J. KAO, X. WANG, J. M. ASHE, D. M. DAVENPORT, and B. C. AMM. Detection of small bleeds in the brain with electrical impedance tomography. *Physiological Measurement* [online]. 2016, **37**(6), 727–750. ISSN 0967-3334. Available at: doi:10.1088/0967-3334/37/6/727

[2] HALLAJI, M., A. SEPPÄNEN, and M. POUR-GHAZ. Electrical impedance tomography-based sensing skin for quantitative imaging of damage in concrete. *Smart Materials and Structures* [online]. 2014, **23**(8), 085001. ISSN 0964-1726. Available at: doi:10.1088/0964-1726/23/8/085001

[3] KOURUNEN, J., R. KÄYHKÖ, J. MATULA, J. KÄYHKÖ, M. VAUHKONEN, and L. M. HEIKKINEN. Imaging of mixing of two miscible liquids using electrical impedance tomography and linear impedance sensor. *Flow Measurement and Instrumentation* [online]. 2008, **19**(6), 391–396. ISSN 0955-5986. Available at: doi:10.1016/j.flowmeasinst.2008.07.002

[4] RYMARCZYK, T., and P. ADAMKIEWICZ. Monitoring damage and dampness in flood embankment by electrical impedance tomography. *Informatyka, Automatyka, Pomiary w Gospodarce i Ochronie Środowiska* [online]. 2017, **7**(1), 59–62. ISSN 2391-6761. Available at: doi:10.5604/01.3001.0010.4584

[5] HOLDER, D. S. *Electrical Impedance Tomography: Methods, History and Applications.* B.m.: CRC Press, 2004. ISBN 978-1-4200-3446-2.

[6] KŘÍŽ, T. *New optimization algorithms for a digital image reconstruction in EIT* [online]. 2015, 73. Doctor of Philosophy. Brno University of Technology. Available at: `https://www.vutbr.cz/www_base/zav_prace_soubor_verejne.php?file_id=113762`.

[7] DĚDKOVÁ, J. *Image reconstruction methods based on electrical impedance tomography.* VUTIUM, 2007. Profesor. Brno University of Technology. ISBN 978-80-214-3384-7.

[8] BORSIĆ, A. *Regularisation Methods for Imaging from Electrical Measurements* [online]. 2002. Doctor of Philosophy. School of Engineering Oxford Brookes University. Available at: `https://radar.brookes.ac.uk/radar/file/4837c97a-d3ff-4521-a1df-f32a378534d2/1/borsic2002regularisationRADAR.pdf`.

[9] BOYLE, A. J. S. *Geophysical Applications of Electrical Impedance Tomography* [online]. B.m., 2016. Doctor of Philosophy. Carleton University. Available at: `https://curve.carleton.ca/8ba36b23-acc0-4ea6-bd6d-b1f98a1b462a`

[10] POLYDORIDES, N. *Image reconstruction algorithms for soft-field tomography* [online]. 2002, 262. Doctor of Philosophy. University of Manchester Institute of Science and Technology. Available at: `http://vummath.ma.man.ac.uk/~bl/theses/npolydorides/thesnick.pdf`.

[11] SILVESTER, P.P., and R.L. FERRARI. *Finite elements for electrical engineers.* 2nd ed. Cambridge: Cambridge University Press, 1990. ISBN 05-213-7219-4.

[12] ADLER, A., and W. R. B. LIONHEART. Uses and abuses of EIDORS: an extensible software base for EIT. *Physiological Measurement* [online]. 2006, **27**(5), S25–S42. ISSN 0967-3334, 1361-6579. Available at: doi:10.1088/0967-3334/27/5/S03

[13] NISSINEN, A. *Modelling Errors in Electrical Impedance Tomography* [online]. Kuopio, 2011, 79. Doctor of Philosophy. University of Eastern Finland. ISBN 978-952-61-0428-7. Available at: `https://erepo.uef.fi/bitstream/handle/123456789/10060/urn_isbn_978-952-61-0428-7.pdf`.

[14] CHENEY, M., D. ISAACSON, and J. NEWELL. Electrical impedance tomography. *Society for Industrial and Applied Mathematics* [online]. SIAM, 1999, **41**(1), 85-101. Available at: `http://homepages.rpi.edu/~newelj/sirev.pdf`

[15] TTAYAGARAJAN, T., M. PONNAVAIKKO, J. SHANMUGAM, R.C. PANDA, and Pg. RAO. Artificial neural networks: principle and application to model based control of drying systems - a review. *Drying Technology* [online]. 1998, **16**(6), 931–966. ISSN 0737-3937, 1532-2300. Available at: doi:10.1080/07373939808917449

[16] GRAUPE, D. *Principles of artificial neural networks.* 3rd edition. New Jersey: World Scientific, 2013. Advanced series on circuits and systems, volume 7. ISBN 978-981-4522-73-1.

[17] BARBOSA, V. A. F., R. R. RIBEIRO, A. R. S. FEITOSA, V. L. B. A. SILVA, A. D. D. ROCHA, R. C. FREITAS, R. E. SOUZA, and W. P. SANTOS. Reconstruction of Electrical Impedance Tomography Using Fish School Search, Non-Blind Search, and Genetic Algorithm. *International Journal of Swarm Intelligence Research (IJSIR)* [online]. 2017, **8**(2), 17–33. ISSN 1947-9263. Available at: doi:10.4018/IJSIR.2017040102

[18] ACHARJYA, D. P., and V. SANTHI, ed. *Bio-inspired computing for image and video processing.* Boca Raton: CRC Press, 2017. ISBN 978-1-4987-6592-3.

[19] NERI, F., and V. TIRRONEN. Recent advances in differential evolution: a survey and experimental analysis. *Artificial Intelligence Review* [online]. 2010, **33**(1–2), 61–106. ISSN 0269-2821, 1573-7462. Available at: doi:10.1007/s10462-009-9137-2

[20] RIBEIRO, R. R., A. R. S. FEITOSA, R. E. DE SOUZA, and W. P. DOS SAN-TOS. A modified differential evolution algorithm for the reconstruction of electrical impedance tomography images. In: *5th ISSNIP-IEEE Biosignals and Biorobotics Conference (2014): Biosignals and Robotics for Better and Safer Living (BRC)* [online]. 2014, 1–6. ISSN 2326-7844. Available at: doi:10.1109/BRC.2014.6880982

[21] RIBEIRO, R. R., A. R. S. FEITOSA, R. E. DE SOUZA, and W. P. DOS SAN-TOS. Reconstruction of electrical impedance tomography images using chaotic self-adaptive ring-topology differential evolution and genetic algorithms. In: *2014 IEEE International Conference on Systems, Man, and Cybernetics (SMC)* [online]. 2014, 2605–2610. ISSN 1062-922X. Available at: doi:10.1109/SMC.2014.6974320

[22] KING, I. ed. *Neural information processing: 13th international conference, ICONIP 2006, Hong Kong, China, October 3-6, 2006: proceedings.* Berlin; New York: Springer, 2006. Lecture notes in computer science, 4232–4234. ISBN 978-3-540-46479-2.

[23] LIONHEART, B. EIT for beginners [online]. 2014, 38. Available at: `http://www2.compute.dtu.dk/~pcha/HDtomo/DTUEIT.pdf`

[24] LIONHEART, W. R. B. EIT reconstruction algorithms: pitfalls, challenges and recent developments. *Physiological Measurement* [online]. 2004, **25**(1), 125–142. ISSN 0967-3334, 1361-6579. Available at: doi:10.1088/0967-3334/25/1/021

[25] BERA, T. K., and J. NAGARAJU. Studying the resistivity imaging of chicken tissue phantoms with different current patterns in Electrical Impedance Tomography (EIT). *Measurement* [online]. 2012, **45**(4), 663–682. ISSN 0263-2241. Available at: doi:10.1016/j.measurement.2012.01.002

[26] LOKE, M. H. Electrical imaging surveys for environmental and engineering studies. *A practical guide to 2-D and 3-D surveys* [online]. 1999. Available at: `http://pages.mtu.edu/~ctyoung/LOKENOTE.PDF`

[27] KOLEHMAINEN, V., M. VAUHKONEN, P. KARJALAINEN, and J. KAIPIO. Assessment of errors in static electrical impedance tomography with adjacent and trigonometric current patterns. *Physiological measurement* [online]. 1997, **18**, 289–303. Available at: doi:10.1088/0967-3334/18/4/003

[28] LIU, K., Y. WU, S. WANG, H. WANG, H. CHEN, B. CHEN, and J. YAO. Artificial Sensitive Skin for Robotics Based on Electrical Impedance Tomography. *Intelligent Systems* [online]. 2020, 1–13. Available at: doi:10.1002/aisy.201900161

[29] WOO, E. J., P HUA, J. WEBSTER, W. TOMPKINS, and R. PALLAS-ARENY. Skin impedance measurements using simple and compound electrodes. *Medical*

& *biological engineering & computing* [online]. 1992, **30**, 97–102. Available at: doi:10.1007/BF02446200

[30] VILHUNEN, T., J. P. KAIPIO, P. J. VAUHKONEN, T. SAVOLAINEN, and M. VAUHKONEN. Simultaneous reconstruction of electrode contact impedances and internal electrical properties: I. Theory. *Measurement Science and Technology* [online]. 2002, **13**(12), 1848–1854. ISSN 0957-0233. Available at: doi:10.1088/0957-0233/13/12/307

[31] HEIKKINEN, L. M., T. VILHUNEN, R. M. WEST, and M. VAUHKONEN. Simultaneous reconstruction of electrode contact impedances and internal electrical properties: II. Laboratory experiments. *Measurement Science and Technology* [online]. 2002, **13**(12), 1855–1861. ISSN 0957-0233. Available at: doi:10.1088/0957-0233/13/12/308

[32] BOVERMAN, G., D. ISAACSON, G. SAULNIER, and J. NEWELL. Methods for Compensating for Variable Electrode Contact in EIT. *IEEE transactions on bio-medical engineering* [online]. 2009, **56**, 2762–72. Available at: doi:10.1109/TBME.2009.2027129

[33] NISSINEN, A., V. KOLEHMAINEN, and J. KAIPIO. Compensation of Modelling Errors Due to Unknown Domain Boundary in Electrical Impedance Tomography. *IEEE transactions on medical imaging* [online]. 2011, **30**, 231–42. Available at: doi:10.1109/TMI.2010.2073716

[34] DARDÉ, J., H. HAKULA, N. HYVÖNEN, and S. STABOULIS. Fine-tuning electrode information in electrical impedance tomography. *Inverse Problems and Imaging* [online]. 2012, **6**. Available at: doi:10.3934/ipi.2012.6.399

[35] DEMIDENKO, E., A. BORSIC, Y. WAN, R. HALTER, and A. HARTOV. Statistical Estimation of EIT Electrode Contact Impedance Using a Magic Toeplitz Matrix. *IEEE Transactions on Biomedical Engineering* [online]. 2011, **58**, 2194–2201. Available at: doi:10.1109/TBME.2011.2125790

[36] HYVÖNEN, N., A. SEPPÄNEN, and S. STABOULIS. Optimizing Electrode Positions in Electrical Impedance Tomography. *SIAM Journal on Applied Mathematics* [online]. 2014, **74**. Available at: doi:10.1137/140966174

[37] SMYL, D., and D. LIU. Optimizing Electrode Positions in 2-D Electrical Impedance Tomography Using Deep Learning. *IEEE Transactions on Instrumentation and Measurement* [online]. 2020, **69**(9), 6030–6044. ISSN 1557-9662. Available at: doi:10.1109/TIM.2020.2970371

[38] ZONG, Z., Y. WANG, and Z. WEI. A Review of Algorithms and Hardware Implementations in Electrical Impedance Tomography (Invited). *Progress In Electromagnetics Research* [online]. 2020, **169**, 59–71. ISSN 1070-4698. Available at: doi:10.2528/PIER20120401

[39] PADILHA LEITZKE, J., and H. ZANGL. A Review on Electrical Impedance Tomography Spectroscopy. *Sensors* [online]. 2020, **20**(18), 5160. Available at: doi:10.3390/s20185160

[40] DUŠEK, J., J. MIKULKA, Z. MŰNSTEROVÁ, and J. PAŘÍLKOVÁ. The Effect of Cylindrical Tank Deformation on Forward Solution in Electrical Impedance Tomography. *EUREKA 2020*. EUREKA. Brno: VUTIUM, Brno University of Technology, 2020. 60-63. ISBN: 978-80-214-5862-8. ISSN: 2464-4595.

[41] DUŠEK, J., and J. MIKULKA. Measurement-Based Domain Parameter Optimization in Electrical Impedance Tomography Imaging. *Sensors* [online]. 2021, **21**(7), 2507. Available at: doi:10.3390/s21072507

[42] DIMAS, Ch., and P. P. SOTIRIADIS. Electrical impedance tomography image reconstruction for adjacent and opposite strategy using FEMM and EIDORS simulation models. In: *2018 7th International Conference on Modern Circuits and Systems Technologies (MOCAST)* [online]. Thessaloniki: IEEE, 2018, 1–4. ISBN 978-1-5386-4788-2. Available at: doi:10.1109/MOCAST.2018.8376604

[43] KRČMAŘÍK, D., M. PETRŮ, and J. KOČÍ. Thorax measurement and analysis using electrical impedance tomography. *Vibroengineering PROCEDIA* [online]. 2019, **26**, 68–73. ISSN 2345-0533. Available at: doi:10.21595/vp.2019.20986

[44] BARA, A., A. SALAMI, K. KOFFI MAWUGNO, A. GUENOUKPATI, O. DJANDJA, and K.-S. BEDJA. Estimation of Soils Electrical Resistivity using ArtificialNeural Network Approach. *American Journal of Applied Sciences* [online]. 2019, **16**, 43–58. Available at: doi:10.3844/ajassp.2019.43.58

[45] DUŠEK, J., J. MIKULKA, M. BALAJKA, J. DĚDKOVÁ, J. PAŘÍLKOVÁ, and Z. MŰNSTEROVÁ. Designing a Cost-Effective Multiplexer for Electrical Impedance Tomography. In: *2019 11th International Congress on Ultra Modern Telecommunications and Control Systems and Workshops (ICUMT)* [online]. 2019, 1–4. ISSN 2157-023X. Available at: doi:10.1109/ICUMT48472.2019.8970696

[46] DUŠEK, J., J. MIKULKA, Z. MŰNSTEROVÁ, and J. PAŘÍLKOVÁ. Designing portable multiplexer for electrical impedance tomography. In *EUREKA 2019 - 7th Colloquium and Working Session*. EUREKA. Brno: Brno University of Technology, VUTIUM, 2019. 86-89. ISBN: 978-80-214-5729-4. ISSN: 2464-4595.

[47] DUŠEK, J., and J. MIKULKA. Electrical Impedance Tomography-Based Spatial Reconstruction of Admittivity in a Cylindrical Object. In: *2020 19th International Conference on Mechatronics - Mechatronika (ME)* [online]. 2020, 1–6. Available at: doi:10.1109/ME49197.2020.9286467

[48] DUŠEK, J., A. VÉJAR, T. RYMARCZYK, and J. MIKULKA. Convergence error exploration for electrical impedance tomography problems with open and closed domains. In: *2018 International Interdisciplinary PhD Workshop (IIPhDW)* [online]. 2018, 39–44. Available at: doi:10.1109/IIPHDW.2018.8388241

[49] DUŠEK, J. Acceleration of Electrical Impedance Tomography Algoritm with Open and Closed Domain Model Evaluation. In *Proceedings of the 24nd Conference STUDENT EEICT 2018*. Brno: 2018. 508-512. ISBN: 978-80-214-5614-3.

[50] VAUHKONEN, M., W. LIONHEART, L. HEIKKINEN, P. VAUHKONEN, and Jari KAIPIO. A matlab package for the EIDORS project to reconstruct two-dimensional EIT images. *Physiological measurement* [online]. 2001, **22**, 107–11. Available at: doi:10.1088/0967-3334/22/1/314

[51] DUŠEK, J., D. HLADKÝ, and J. MIKULKA. Electrical impedance tomography methods and algorithms processed with a GPU. In: *2017 Progress In Electromagnetics Research Symposium - Spring (PIERS)* [online]. 2017, 1710–1714. Available at: doi:10.1109/PIERS.2017.8262025

[52] DUŠEK, J., and J. MIKULKA. Using a GPU to Accelerate Electrical Impedance Tomography Algorithms. In *Proceedings of IIPhDW 2017 in Lodz*. Lodz, Polsko: 2017. 59-63. ISBN: 978-83-7283-858-2.

[53] DUŠEK, J., J. MIKULKA, Z. MŰNSTEROVÁ, and J. PAŘÍLKOVÁ. System for conductivity reconstruction of soil sample based on electrical impedance tomography. In *EUREKA 2019 - 7th Colloquium and Working Session*. EUREKA. Brno: Brno University of Technology, VUTIUM, 2019. 90-92. ISBN: 978-80-214-5729-4. ISSN: 2464-4595.

[54] DUŠEK, J., J. MIKULKA, J. PAŘÍLKOVÁ, and Z. MŰNSTEROVÁ. Reconstruction of the real and imaginary parts of tank model admittance via electrical impedance tomography. *Elektrorevue*. 2019, **21**(2), 1-7. ISSN: 1213-1539. Available at: http://www.elektrorevue.cz

Curriculum vitae

Name and surname: Jan Dušek, M.Sc.

Date of birth: 3. 1. 1992

Phone: +420 605 385 125

E-mail addresses: xdusek19@vut.cz

j.d.mikro@gmail.com

Education

9/2016 – present	Brno University of Technology, Faculty of Electrical Engineering and Communication (FEEC), Department of Theoretical and Experimental Electrical Engineering (DTEEE) Doctoral study Thesis: *Optimizing Algorithms in Electrical Impedance Tomography*
9/2014 – 6/2016	Brno University of Technology, FEEC M.Sc. in microelectronics Thesis: *Reactive sputtering of Al_2O_3*
9/2011 – 6/2014	Brno University of Technology, FEEC B.Sc. in microelectronics and technology Thesis: *Control of reactive magnetron sputtering*

Practical experience

1/2017 – present	Brno University of Technology, FEEC, DTEEE Technician, Ph.D. student Lecturer in electrical engineering and measurement
9/2017 – 1/2018	Netrix S.A., Zwiazkowa 26, 20-148 Lublin, Poland Erasmus internship at a research and development center The results were published at the IIPhDW 2018 conference
7/2016 – 8/2017	Codasip s.r.o., Technická 2935/23, Brno UVM verification of digital buses Designing and developing a Bk7 processor
5/2012 – 6/2016	Institute of Scientific Instruments of the Czech Academy of Sciences, Královopolská 147, Brno Science assistant Plasma enhanced chemical vapour deposition of thin films Automating and controling the deposition process

Training and skills

9/2019 – 8/2020	Brno University of Technology, Institute of Forensic Engineering
	Expertise: *Laboratory apparatus and metrology*
9/2016 – 9/2017	CEITEC Nano Research Infrastructure;
	Electron microscopy practicals

Conferences and workshops

- Conferences: ICUMT (Dublin; 2019), IIPhDW (Łodz, Świnoujsćie; 2017, 2018), Mechatronics (Praha; 2020), EEICT (Brno; 2016, 2018)
- Workshop: Engineering applications of information technologies (Lublin – Warsaw; 2017)

Projects

- Junior grant: *Detection of ground-based environmental anomalies via electrical impedance tomography*; a BUT internal grant project leader (3/2018 – 2/2019)

Instruction and lecturing

- Electrical engineering and measurement
- Organizing student competitions (*Mikrokontroléry letí*) at BUT since 2018
  - Sponsoring negotiations; funding responsibility; overall management

Other achievements

- 2016: Winner of the EEICT student contest (the microelectronics and technology section)
- 2014: Dean's award for an outstanding Bachelor thesis
- 2012: Runner-up in the *Measurement for the Digital Future* contest